

Detection of Na in WASP-21b's lower and upper atmosphere

G. Chen¹, N. Casasayas-Barris^{2,3}, E. Pallé^{2,3}, L. Welbanks⁴, N. Madhusudhan⁴, R. Luque^{2,3}, and F. Murgas^{2,3}

¹ Key Laboratory of Planetary Sciences, Purple Mountain Observatory, Chinese Academy of Sciences, Nanjing 210023, PR China
e-mail: guochen@pmo.ac.cn

² Instituto de Astrofísica de Canarias, Vía Láctea s/n, E-38205 La Laguna, Tenerife, Spain

³ Departamento de Astrofísica, Universidad de La Laguna, Spain

⁴ Institute of Astronomy, University of Cambridge, Madingley Road, Cambridge CB3 0HA, UK

Received Month 00, 2020; accepted Month 00, 2020

ABSTRACT

Optical transmission spectroscopy provides crucial constraints on the reference pressure levels and scattering properties for hot Jupiter atmospheres. For certain planets, where alkali atoms are detected in the atmosphere, their line profiles could serve as a good probe to link upper and lower atmospheric layers. WASP-21b is a Saturn-mass hot Jupiter orbiting a thick disc star, with a low density and an equilibrium temperature of 1333 K, which makes it a good target for transmission spectroscopy. Here, we present a low-resolution transmission spectrum for WASP-21b based in one transit observed by the OSIRIS spectrograph at the 10.4 m Gran Telescopio Canarias (GTC), and a high-resolution transmission spectrum based in three transits observed by HARPS-N at Telescopio Nazionale Galileo (TNG) and HARPS at the ESO 3.6 m telescope. We performed spectral retrieval analysis on GTC's low-resolution transmission spectrum and report the detection of Na at a confidence level of $>3.5\sigma$. The Na line exhibits a broad line profile that can be attributed to pressure broadening, indicating a mostly clear planetary atmosphere. The spectrum shows a tentative excess absorption at the K D₁ line. Using HARPS-N and HARPS, we spectrally resolved the Na doublet transmission spectrum. An excess absorption at the Na doublet is detected during the transit, and shows a radial velocity shift consistent with the planet orbital motion. We proposed a metric to quantitatively distinguish hot Jupiters with relatively clear atmospheres from others, and WASP-21b has the largest metric value among all the characterized hot Jupiters. The detection of Na at both lower and upper atmosphere of WASP-21b reveals that it is an ideal target for future follow-up observations, providing the opportunity to understand the nature of its atmosphere across a wide range of pressure levels.

Key words. Planetary systems – Planets and satellites: individual: WASP-21b – Planets and satellites: atmospheres – Techniques: spectroscopic

1. Introduction

Transmission spectroscopy (Seager & Sasselov 2000; Brown 2001) is one of the most efficient techniques to characterize exoplanet atmospheres. The slant viewing geometry makes it extremely sensitive to opacity sources in the atmospheres (Fortney 2005), resulting in detections of a variety of atoms, ions, and molecules in dozens of exoplanets (e.g., Sing et al. 2016; Tsiaras et al. 2018; Madhusudhan 2019). Consequently, trends start to emerge in the derived chemical abundances and metallicities, which could connect to planet formation histories (e.g., Kreidberg et al. 2014; Madhusudhan et al. 2014, 2017; Wakeford et al. 2017; Pinhas et al. 2019; Welbanks et al. 2019).

However, given the degeneracy between reference pressure and chemical abundances (Benneke & Seager 2012; Griffith 2014; Heng & Kitzmann 2017), ubiquitous clouds and hazes strongly degrade our capability to precisely retrieve detailed atmospheric nature (Stevenson 2016; Iyer et al. 2016; Heng 2016; Crossfield & Kreidberg 2017; Fu et al. 2017). One way to break the degeneracy is to search for the pressure broadening signature of alkali lines (Griffith 2014; Heng & Kitzmann 2017; MacDonald & Madhusudhan 2017; Welbanks & Madhusudhan 2019), in particular Na and K, which, when resolved at high spectral resolution, could also help characterize planetary wind and give insight into heating and cooling processes in the upper atmosphere (Louden & Wheatley 2015; Huang et al. 2017; Seidel et al. 2020;

Gebek & Oza 2020). Recently, several hot Jupiters have been found to exhibit broad line profiles, at the Na or K lines, that can be associated with pressure broadening (e.g., Nikolov et al. 2018; Chen et al. 2018; Pearson et al. 2019). All these planets seem to have equilibrium temperatures clustered between 1200 K and 1500 K.

Here we present low- and high-resolution transit observations of the Saturn-mass hot Jupiter WASP-21b. This low-density planet has an equilibrium temperature of $T_{\text{eq}} = 1333 \pm 28$ K and a low surface gravity of $g_p = 5.07 \pm 0.35$ m s⁻¹ (Ciceri et al. 2013), which could potentially exhibit a transit depth variation of 251 ppm per scale height, making it a good target for atmospheric characterization via transmission spectroscopy. WASP-21b orbits a G3V thick disc star in a circular orbit every 4.32 days (Bouchy et al. 2010), which is one of the most metal-poor planet hosts ($[\text{Fe}/\text{H}] = -0.46 \pm 0.11$). Barros et al. (2011) analyzed three transits, two of which are partial transits, obtained with the robotic 2.0 m Liverpool Telescope, and found that the host star is evolving off the main sequence. They revised down the stellar mass and hence obtained a lower planet mass. Southworth (2012) reanalyzed the data of Barros et al. (2011) in the homogeneous studies of 38 planets, and derived a stellar mass closer to Bouchy et al. (2010) but a stellar radius larger than both Bouchy et al. (2010) and Barros et al. (2011). Ciceri et al. (2013) observed a new single transit with both 1.5 m Cassini Telescope and 1.2 m Calar Alto Telescope, and presented the lat-

arXiv:2007.13429v1 [astro-ph.EP] 27 Jul 2020

est revised physical parameters. They derived $0.890 \pm 0.079 M_{\odot}$ and $1.136 \pm 0.051 R_{\odot}$ for the host star, and $0.276 \pm 0.019 M_{\text{jup}}$ and $1.162 \pm 0.054 R_{\text{jup}}$ for the planet. Finally, [Seeliger et al. \(2015\)](#) added another three new transit observations and found no hints of significant transit timing variations.

This paper is organized as follows. In Sect. 2, we summarize the low- and high-resolution transit observations and detail the data reduction. In Sect. 3, we present the light-curve analysis for the low-resolution data, and describe the spectral retrieval analysis. In Sect. 4, we present the analyses on radial velocities and high-resolution transmission spectroscopy. In Sect. 5, we discuss the properties of WASP-21b’s atmosphere inferred from transmission spectrum, and put it in the context of all hot Jupiters that have been characterized by low-resolution optical transmission spectroscopy. Conclusions are given in Sect. 6.

2. Observations and data reduction

To derive the transmission spectrum for WASP-21b, we observed one transit at low spectral resolution and one transit at high spectral resolution. We also collected archival data for another two transits observed at high spectral resolution. The low-resolution observation was carried out in seeing-limited conditions, along with a reference star, while the high-resolution observations were single-object only, without flux calibration. The summary of the five transit observations is given in Table 1.

2.1. GTC/OSIRIS

One transit of WASP-21b was observed on the night of September 11, 2012 (program GTC47-12B, PI: E. Pallé), using the OSIRIS spectrograph ([Sánchez et al. 2012](#)) installed at the 10.4 m Gran Telescopio CANARIAS (GTC) in La Palma, Spain. The observation was performed with the R1000R grism through the 12'' slit. The R1000R grism can cover a wavelength range of 510–1000 nm at a spectral resolution of $\mathcal{R} \sim 1122$. The long-slit allows a reference star to be simultaneously observed with the target star WASP-21 ($r' = 11.4$ mag). The adopted reference star 2MASS J23094822+1822564 ($r' = 11.6$ mag) was 2.5' away. Both stars were placed on CCD chip 2, while CCD chip 1 was switched off. The CCD was configured in the 2×2 binning mode (0.254'' per binned pixel) with a readout speed of 200 kHz.

The observation lasted 4.1 hours, and missed the pre-transit baseline while included 42 min of post-transit baseline. The first eleven frames had an exposure time of 30 sec, while the remaining used 22 sec. A total of 313 frames were recorded. The resulting duty cycle is 47.1%. The weather was not clear all the time. The stars might have passed thin cirrus for ~ 1.1 hours after mid-transit, during which the target and reference stars showed similar flux variation. During the whole observation, the airmass dropped monotonically from 1.928 to 1.017. The seeing varied between 0.73'' and 1.78'', which was measured as the full width at half maximum (FWHM) of the spatial profile at the central wavelength. This resulted in a seeing-limited spectral resolution of roughly 10 Å. The centroids of the spatial profile drifted around 2 pixels, while no clear drift trend was observed in the cross-dispersion direction.

The spectral images were calibrated following the same method adopted in [Chen et al. \(2017a,b, 2018\)](#), including over-scan and bias subtraction, flat correction, and sky removal. The one-dimensional spectra were extracted using an aperture diameter of 42 pixels, which gave the lowest scatter in the white-color light curve. The time stamp was converted to Barycen-

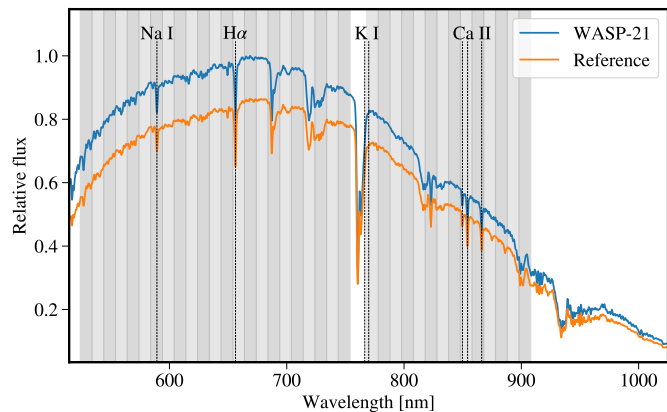


Fig. 1. Median-combined out-of-transit stellar spectra of WASP-21 (blue) and the reference star (orange), obtained with the R1000R grism of GTC/OSIRIS on the night of September 11, 2012. The spectra have been individually normalized, with the target-to-reference flux ratio being preserved. The color-shaded areas indicate the divided passbands that are used to create the spectroscopic light curves.

tric Julian Date in the Barycentric Dynamical Time standard (BJD_{TDB} ; [Eastman et al. 2010](#)). The white-color light curve was integrated between 524 nm and 908 nm, except that 754–768 nm was excluded to avoid the strong noise introduced by the telluric oxygen-A band. The spectral light curves were integrated in 10 nm bin width. The wavelengths longer than 908 nm were not used owing to significant fringing effects. Figure 1 shows the median-combined out-of-transit stellar spectra and the adopted spectral band passes.

2.2. TNG/HARPS-N

One transit of WASP-21b was observed on the night of September 7, 2018 (program CAT18A_D1, PI: G. Chen) using the HARPS-N spectrograph ([Cosentino et al. 2014](#)) installed at the 3.58 m Telescopio Nazionale Galileo (TNG) in La Palma, Spain. HARPS-N is a fiber-fed echelle spectrograph, covering a wavelength range of 383–693 nm at a spectral resolution of $\mathcal{R} \sim 115\,000$. One of the two HARPS-N fibers (fiber A) was pointed to the target star WASP-21, and the other (fiber B) was pointed to sky to monitor the telluric emission. The observation lasted 8.4 hours, and covered the whole transit. The exposure time was 900 sec, resulting in 33 frames, of which 11 frames were fully in-transit (i.e., between the second and third contacts of a transit) and 19 frames were fully out-of-transit (i.e., no overlap with the transit during the exposure). The signal-to-noise ratio (S/N) varied between 23 and 45 at the continuum around 5888 Å, while it decreased to $S/N \sim 7$ –13 at the Na D₂ line core.

The data were reduced by the version 3.7 of the HARPS-N data reduction software. In the subsequent analysis, we will use the pipeline-reduced order-merged one-dimensional spectra, labeled as s1d by the pipeline. The wavelengths have been corrected for the barycentric Earth radial velocity, and have been re-sampled in a step of 0.01 Å. Strong interstellar Na absorption can be seen in the WASP-21 spectra. Fortunately, the systemic radial velocity of WASP-21 is well away from zero (-89.45 km s^{-1} , [Bouchy et al. 2010](#), also see Sect. 4.1), shifting the stellar Na well separated from interstellar Na. The interstellar Na were masked in the subsequent analysis. The telluric Na emission was close to the interstellar Na, which was simultaneously masked.

Table 1. Observation summary.

#	Telescope	Instrument	Start Night	UT window	T_{exp} [s]	N_{obs}	Airmass ^(a)	S/N ^(b)		Program
								Cont.	Core	
1	ESO 3.6 m	HARPS	2011-09-05	02:37-08:18	900	22	1.94-1.48-2.33	29-37	8-11	087.C-0649(A)
2	ESO 3.6 m	HARPS	2011-09-18	01:44-06:54	900	19	1.96-1.48-1.98	21-29	6-9	087.C-0649(A)
3	TNG	HARPS-N	2018-09-07	21:37-06:00	900	33	1.58-1.02-2.15	23-45	7-13	CAT18A_D1
4	GTC	OSIRIS	2012-09-11	20:41-00:48	22	313	1.93-1.02-1.02	–	–	GTC47-12B

Notes. ^(a) The first and third values refer to the airmass at the beginning and at the end of the observation. The second value gives the minimum airmass. ^(b) The two values correspond to the minimum and maximum signal-to-noise ratio (S/N), respectively. The S/N of the continuum was measured at around 5888 Å. The S/N of the Na core was measured at the D₂ line.

Therefore, we did not use fiber B to correct the telluric emission in fiber A.

2.3. ESO 3.6 m/HARPS

The archival data for two transits of WASP-21b were collected from the ESO archive under the program 087.C-0649(A) (PI: A. Triaud). The two transits covered the complete transit event, which were observed on the nights of September 5, 2011 and September 18, 2011, respectively. The observations were made with the HARPS spectrograph (Mayor et al. 2003) installed at the ESO 3.6 m telescope in La Silla, Chile. As the design predecessor of HARPS-N, HARPS also has a spectral resolution of $\mathcal{R} \sim 115\,000$ and covers a wavelength range of 378–691 nm. For the two archival transits, only the data collected by the fiber A were available. An exposure time of 900 sec was adopted for the two transits. The first transit was observed for 5.7 hours, with 22 frames being collected, of which 11 were fully in-transit and 8 were fully out-of-transit. The second transit was observed for 5.2 hours, with 19 frames being collected, of which 11 were fully in-transit and 6 were fully out-of-transit. The S/N of the HARPS spectra were similar to those of the HARPS-N spectra, but with slightly lower values due to higher airmass visible from the Southern hemisphere. The data were reduced by the version 3.5 of the HARPS data reduction software. The pipeline products are similar to the HARPS-N ones.

3. Low-resolution data analysis

3.1. GTC/OSIRIS light-curves

The GTC/OSIRIS transit light curves were modeled following the method described in Chen et al. (2018), where Gaussian processes (GP; Rasmussen & Williams 2006; Gibson et al. 2012) were employed to account for the correlated noise. The Mandel & Agol (2002) analytic transit model and GP were implemented by the Python packages batman (Kreidberg 2015) and george (Ambikasaran et al. 2015), respectively. The Bayesian parameter estimation was implemented by the Python package emcee (Foreman-Mackey et al. 2013).

We adopted the quadratic limb darkening law for the analytic transit model. The limb darkening coefficients (u_1, u_2) were fitted with Gaussian priors $\mathcal{N}(u_i, \sigma_{u_i}^2)$ for both white and spectral light curves. The prior mean values (u_i) were derived using the Kurucz ATLAS9 stellar atmosphere models with stellar effective temperature $T_{\text{eff}} = 5750$ K, surface gravity $\log g_{\star} = 4.5$, and metallicity $[\text{Fe}/\text{H}] = -0.5$ (Espinoza & Jordán 2015), which is the closest grid to the stellar parameters of WASP-21 (Bouchy

Table 2. Adopted parameters for the WASP-21 system.

Parameter	Value
<i>Stellar Parameters</i>	
Stellar mass, M_{\star} [M_{\odot}]	0.890 ± 0.079 ^(a)
Stellar radius, R_{\star} [R_{\odot}]	1.136 ± 0.051 ^(a)
Effective temperature, T_{eff} [K]	5800 ± 100 ^(b)
Surface gravity, $\log g_{\star}$ [cgs]	4.277 ± 0.026 ^(a)
Metallicity, [Fe/H]	-0.46 ± 0.11 ^(b)
Proj. rotation velocity, $v \sin i_{\star}$ [km s^{-1}]	1.5 ± 0.6 ^(b)
<i>Planet Parameters</i>	
Planet mass, M_p [M_J]	0.276 ± 0.019 ^(a)
Planet radius, R_p [R_J]	1.162 ± 0.054 ^(a)
Equilibrium temperature, T_{eq} [K]	1333 ± 28 ^(a)
Surface gravity, $\log g_p$ [cgs]	2.71 ± 0.03 ^(a)
<i>Orbital Parameters</i>	
Semi-major axis, a [AU]	0.0499 ± 0.0015 ^(a)
Eccentricity, e	0 (fixed) ^(b)
RV semi-amplitude, K_{\star} [km s^{-1}]	0.0372 ± 0.0011 ^(b)

References. ^(a) Ciceri et al. (2013). ^(b) Bouchy et al. (2010).

et al. 2010, also see our Table 2). The prior standard deviation values were $\sigma_{u_i} = 0.1$ for the white light curve, and the width of the model grid gap for the spectral light curves. The grid gap was estimated by comparing the set of $T_{\text{eff}} = 5750$ K to another two sets of values calculated at $T_{\text{eff}} = 5500$ K and $T_{\text{eff}} = 6000$ K, where the larger difference was recorded.

We employed the squared exponential (SE) kernel for the GP covariance matrix,

$$k_{\text{SE}}(x_i, x_j, \theta) = A^2 \exp \left[- \sum_{\alpha=1}^N \left(\frac{x_{\alpha,i} - x_{\alpha,j}}{L_{\alpha}} \right)^2 \right]. \quad (1)$$

For the white-color light curve, we used the analytic transit model \mathcal{T}_w as the mean function of the GP, with inclination i , scale semi-major axis a/R_{\star} , radius ratio R_p/R_{\star} , mid-transit time T_{mid} , u_1 , and u_2 as the free parameters. Corresponding GP input variables $x_{i,j}$ were time sequence t , spatial position drift y and spatial seeing variation s_y . After the light-curve modeling, we divided the white-color light curve by the best-fitting transit model \mathcal{T}_w to derive the common-mode trend \mathcal{S}_w , and then divided every spectral light curve by \mathcal{S}_w to correct for this common-

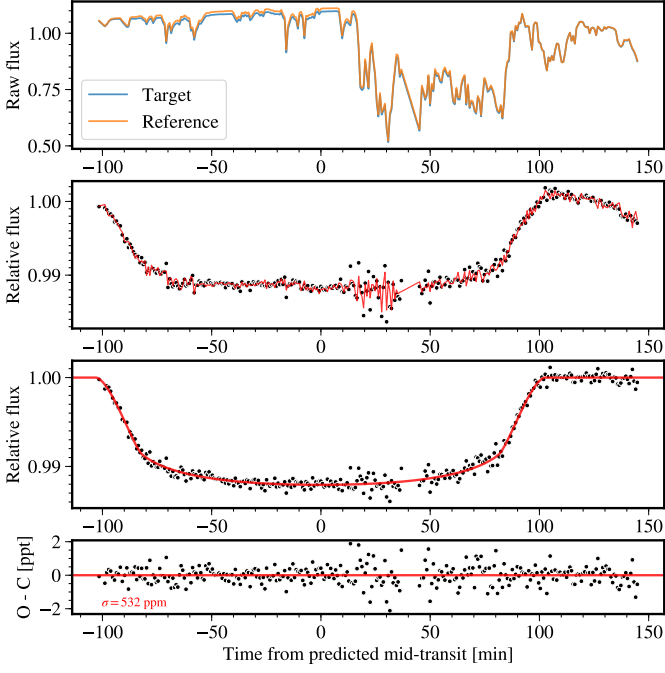


Fig. 2. White-color light curve obtained with GTC/OSIRIS. From top to bottom are *i*) raw flux time series divided by exposure time, *ii*) raw light curve (i.e., normalized target-to-reference flux ratios), *iii*) light curve corrected for systematics, and *iv*) best-fit residuals. The red line shows the best-fit model. The gap at around +40 min is due to missing raw files in the data archive.

Table 3. Derived parameters from GTC/OSIRIS white light curve.

Parameter	Value
<i>Free parameters</i>	
Radius ratio, R_p/R_\star	$0.1016^{+0.0015}_{-0.0014}$
Orbital inclination, i [deg]	$88.28^{+0.90}_{-0.69}$
Scaled semi-major axis, a/R_\star	$10.23^{+0.36}_{-0.40}$
Linear limb-darkening coeff., u_1	0.294 ± 0.063
Quad. limb-darkening coeff., u_2	0.364 ± 0.090
Mid-transit time, T_{mid} [MJD ^(a)]	56181.93874 ± 0.00031
<i>Derived parameters</i>	
Transit duration, T_{14} [d]	$0.1426^{+0.0013}_{-0.0012}$
Fully in-transit duration, T_{23} [d]	$0.1137^{+0.0017}_{-0.0021}$
<i>Revised ephemeris</i>	
Transit epoch, T_0 [MJD ^(a)]	54742.54198 ± 0.00068
Orbital period, P [d]	4.3225130 ± 0.0000021

Notes. ^(a) MJD = BJD_{TDB} - 2400000.5.

mode trend. To model the corrected spectral light curves, we used the analytic transit model multiplied by a baseline function $\mathcal{T}_{\text{spec}}(c_0 + c_1t + c_2t^2)$ as the mean function. The free transit parameters were R_p/R_\star , u_1 , and u_2 , while the others were fixed to the white light-curve values (see Table 3). In this case, the GP input variables $x_{i,j}$ were y and s_y . All the GP hyperparameters were fit with uniform priors. The time scale hyperparameter L_t is always forced to be no shorter than WASP-21b’s ingress/egress duration (0.01445 days).

Table 4. Derived GTC/OSIRIS transmission spectrum.

#	λ_{start} [nm]	λ_{end} [nm]	R_p/R_\star
1	524	534	$0.0996^{+0.0013}_{-0.0012}$
2	534	544	$0.1006^{+0.0012}_{-0.0013}$
3	544	554	$0.1003^{+0.0013}_{-0.0013}$
4	554	564	$0.1035^{+0.0013}_{-0.0012}$
5	564	574	$0.1033^{+0.0011}_{-0.0011}$
6	574	584	$0.1049^{+0.0011}_{-0.0011}$
7	584	594	$0.1087^{+0.0017}_{-0.0017}$
8	594	604	$0.1051^{+0.0011}_{-0.0012}$
9	604	614	$0.1049^{+0.0011}_{-0.0011}$
10	614	624	$0.1024^{+0.0013}_{-0.0014}$
11	624	634	$0.1052^{+0.0011}_{-0.0011}$
12	634	644	$0.1043^{+0.0011}_{-0.0012}$
13	644	654	$0.1026^{+0.0011}_{-0.0011}$
14	654	664	$0.1026^{+0.0011}_{-0.0012}$
15	664	674	$0.1025^{+0.0012}_{-0.0012}$
16	674	684	$0.1003^{+0.0012}_{-0.0012}$
17	684	694	$0.1036^{+0.0011}_{-0.0011}$
18	694	704	$0.1003^{+0.0012}_{-0.0013}$
19	704	714	$0.1029^{+0.0012}_{-0.0012}$
20	714	724	$0.1012^{+0.0013}_{-0.0013}$
21	724	734	$0.1004^{+0.0013}_{-0.0012}$
22	734	744	$0.1022^{+0.0012}_{-0.0012}$
23	744	754	$0.1017^{+0.0013}_{-0.0014}$
24	768	778	$0.1027^{+0.0013}_{-0.0013}$
25	778	788	$0.0998^{+0.0012}_{-0.0013}$
26	788	798	$0.1022^{+0.0012}_{-0.0012}$
27	798	808	$0.1019^{+0.0013}_{-0.0012}$
28	808	818	$0.1008^{+0.0017}_{-0.0015}$
29	818	828	$0.0995^{+0.0014}_{-0.0014}$
30	828	838	$0.1047^{+0.0014}_{-0.0013}$
31	838	848	$0.1022^{+0.0014}_{-0.0016}$
32	848	858	$0.1014^{+0.0016}_{-0.0017}$
33	858	868	$0.1007^{+0.0017}_{-0.0017}$
34	868	878	$0.1004^{+0.0017}_{-0.0017}$
35	878	888	$0.0989^{+0.0023}_{-0.0022}$
36	888	898	$0.1000^{+0.0022}_{-0.0022}$
37	898	908	$0.1013^{+0.0034}_{-0.0035}$

The transit parameters derived from the white-color light curve are given in Table 3. The derived GTC/OSIRIS transmission spectrum is presented in Table 4. The white-color light curve and spectral light curves are shown in Fig. 2 and Fig. 3, respectively. The resulting standard deviation of the best-fitting light-curve residuals is 532 ppm, which is 6.1 times the photon noise. In contrast, the standard deviation of the spectral light-curve residuals is 1.07–1.44 times the photon noise. The large

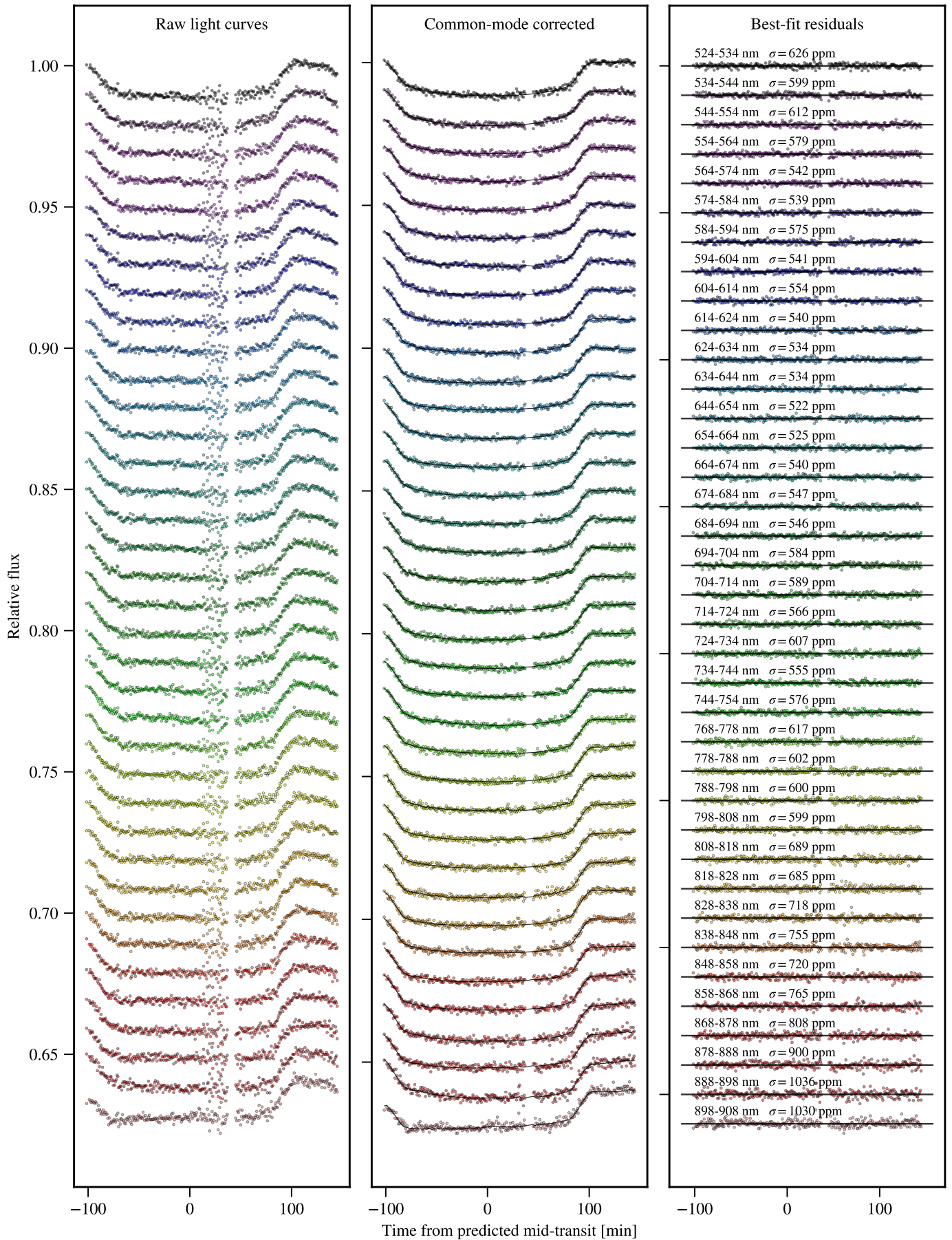


Fig. 3. Spectroscopic light curves of WASP-21b obtained with the R1000R grism of GTC/OSIRIS before (*left panel*) and after removing the common-mode systematics (*middle panel*), along with the best-fit residuals (*right panel*).

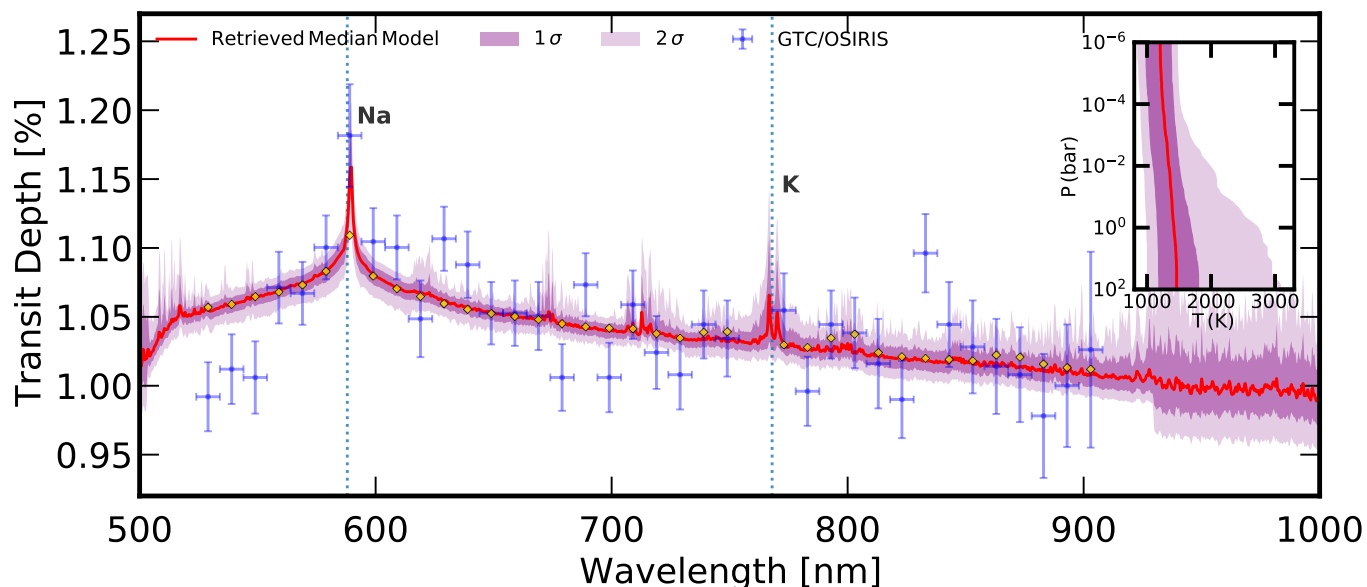


Fig. 4. WASP-21b’s transmission spectrum and retrieved models. The blue crosses are the error bars and bin width of the observed spectrum by GTC/OSIRIS. It shows a strong absorption peak at ~ 589 nm. This feature is preferentially explained by our retrieval models by including the opacity resulting from Na. We show in an inset the retrieved P-T profile for the data using our fiducial model. The red curve shows the retrieved median model while the purple shaded areas show the 1σ and 2σ confidence regions. The yellow diamonds show the binned version for the retrieved median model.

value above photon noise for the white-color light curve is likely a result of the poor weather conditions (e.g., cloud crossing as seen in the raw flux time series). The time-dependent light-curve scatter is mostly common-mode, which was artificially reduced in the corrected spectral light curves when removing the common-mode trend.

3.2. GTC/OSIRIS transmission spectrum

3.2.1. Spectral retrieval analysis

The GTC transmission spectrum of WASP-21b is shown in Figure 4. We performed a retrieval analysis to constrain the atmospheric properties of the planet at the day-night terminator region. Our atmospheric retrieval code was adapted from the works of Pinhas et al. (2018) as used in previous studies (e.g., Chen et al. 2018; Welbanks et al. 2019). Our code computes line-by-line radiative transfer in a transmission geometry assuming a plane parallel planetary atmosphere in hydrostatic equilibrium. Our model retrieves the pressure-temperature (P-T) profile of the atmosphere utilizing the six-parameter prescription of Madhusudhan & Seager (2009) in an atmosphere that spans from 10^2 to 10^{-6} bar.

In the retrieval framework the volumetric mixing ratios of the chemical species in the atmosphere are free parameters and assumed to be constant. We consider absorption due to molecules and atomic species that could be present in hot Jupiter atmospheres (Madhusudhan et al. 2016). The chemical opacity sources considered in this work are H_2 - H_2 and H_2 -He collision induced absorption (CIA; Richard et al. 2012), CH_4 (Yurchenko & Tennyson 2014), CO (Rothman et al. 2010), CO_2 (Rothman et al. 2010), H_2O (Rothman et al. 2010), HCN (Barber et al. 2014), K (Allard et al. 2016), Na (Allard et al. 2019), NH_3 (Yurchenko et al. 2011), TiO (Schwenke 1998), AlO (Patrascu et al. 2015), and VO (McKemmish et al. 2016). The opacities for the chemical species are computed following the methods of

Gandhi & Madhusudhan (2017) and with H_2 -broadened Na and K cross sections as explained in Welbanks et al. (2019).

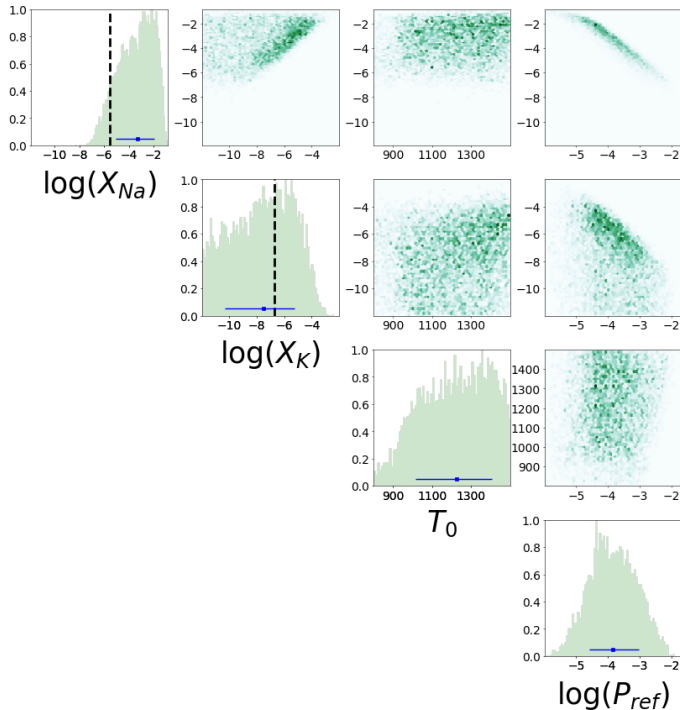
Our models consider the possibility of inhomogeneous cloud and haze cover using the parametrization of MacDonald & Madhusudhan (2017). The model considers cloudy regions of the atmosphere to consist of an opaque cloud deck with a cloud-top pressure P_{cloud} in units of bar and scattering due to hazes above the clouds. In the parametrization, hazes are included as $\sigma = a\sigma_0(\lambda/\lambda_0)^\gamma$, where γ is the scattering slope, a is the Rayleigh-enhancement factor, and σ_0 is the H_2 Rayleigh scattering cross-section at a reference wavelength. The inhomogeneous clouds and scattering hazes are included through the parameter ϕ , which is the cloud/haze fraction cover in the planet’s atmosphere. The Bayesian inference and parameter estimation is conducted using the nested sampling algorithm implemented via the MultiNest application (Feroz et al. 2009) through the Python interface PyMultiNest (Buchner et al. 2014).

We perform an initial exploratory retrieval considering possible absorption due to all 11 chemical species considered in this work, inhomogeneous cloud and haze cover, and a parametric P-T profile. As expected, we find that the only chemical species relatively constrained by the data are those with strong spectroscopic signatures in the optical wavelengths. Therefore we determine our fiducial model to consider absorption due to H_2O , Na, K, TiO, AlO and VO only, as well as a parametric P-T profile and inhomogeneous cloud and haze cover. The fiducial model has a total of 17 parameters: 6 chemical abundances, 6 parameters for the P-T profile, 4 parameters for the cloud and haze prescription, and 1 parameter for the reference pressure corresponding to the reference planetary radius of $1.162 R_J$.

Figure 4 shows the retrieved median model to the observations along with the 1σ and 2σ confidence regions. It also shows in an inset the retrieved pressure-temperature profile for the fiducial model. Our results suggest that the features in the spectrum can be explained by the presence of Na in the planet’s atmosphere. Using the fiducial model as reference we report a possi-

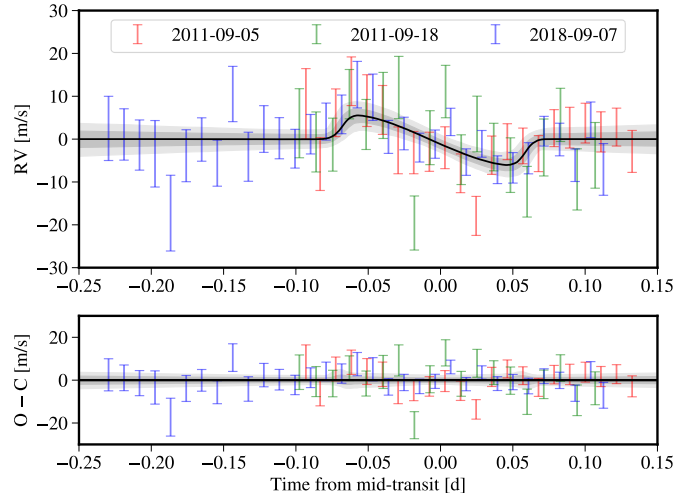
Table 5. Summary of GTC/OSIRIS retrieval results.

Model	$\log_{10}(X_{\text{Na}})$	Na detection significance	$\log_{10}(X_{\text{K}})$	$\ln(\mathcal{Z})$	$\bar{\chi}^2$
Fiducial	$-2.57^{+0.84}_{-1.24}$	$3.5\text{-}\sigma$	$-7.42^{+2.22}_{-2.65}$	235.79	2.25
Simplified	$-3.31^{+1.34}_{-1.77}$	$4.9\text{-}\sigma$	$-7.53^{+2.26}_{-2.80}$	239.12	1.42


Fig. 5. Posterior distribution for the simplified model retrieval of WASP-21b's transmission spectrum. This four parameter model is the highest evidence model and considers absorption due to Na and K only in a clear isothermal atmosphere. Na and K solar abundance expectations are shown using black dashed lines.

ble detection of Na at a confidence level of $3.5\text{-}\sigma$. The retrieved Na abundance is $\log_{10}(X_{\text{Na}}) = -2.57^{+0.84}_{-1.24}$. Besides Na, K also shows possible spectroscopic signatures at ~ 770 nm. Our models do not exhibit a strong preference for the presence of K in the spectrum of WASP-21b and derive a largely unconstrained abundance of $\log_{10}(X_{\text{K}}) = -7.42^{+2.22}_{-2.65}$. Similarly, the data does not provide strong constraints on the P-T profile or the presence of clouds and hazes in the atmosphere of WASP-21b. The retrieved cloud and haze parameters are unconstrained and consistent with a mostly clear atmosphere, partly due to the lack of features in the data indicating a scattering slope. The P-T profile remains largely unconstrained with a derived temperature at 100 mbar, close to the photosphere, of $T_{100\text{ mbar}} = 1371^{+254}_{-230}$ K consistent with the equilibrium temperature of the planet.

Given that current spectroscopic observations do not place strong constraints on the P-T profile or the presence of clouds and hazes we consider a simplified model retrieval. The simplified model considers absorption due to Na and K only, an isothermal P-T profile, and a clear atmosphere. The simplified model retrieved abundances are $\log_{10}(X_{\text{Na}}) = -3.31^{+1.34}_{-1.77}$ and $\log_{10}(X_{\text{K}}) = -7.53^{+2.26}_{-2.80}$, consistent with the fiducial model. The derived Na abundance is marginally consistent with expectations from solar abundance chemistry of $\log_{10}(\text{Na}/\text{H}) = -5.76$ (Asplund et al. 2009). Similarly, the retrieved temperature for the


Fig. 6. The Rossiter-McLaughlin effect in the radial velocity curve of WASP-21. The transits observed on the nights of September 5, 2011, September 18, 2011, and September 7, 2018 are shown in red, green, and blue, respectively. The median RM model and its $1\text{-}\sigma$ and $2\text{-}\sigma$ confidence regions are shown in black and gray. Top panel shows the anomaly caused by the RM effect. Bottom panel shows the residuals after removing the median RM model.

isotherm is $T = 1224^{+181}_{-208}$ K, consistent with the equilibrium temperature and the derived temperature at 100 mbar in the fiducial model. Using this simplified model as reference, Na is detected at a confidence level of $4.9\text{-}\sigma$. The posterior distribution for this retrieval is shown in Fig. 5 and our retrieval results summarized in Table 5.

3.2.2. A search of narrow alkali features

We also examined the 16 \AA bin transmission spectrum zoomed at the Na and K doublets (see Fig. A.1 in Appendix A). The narrow-band transmission spectrum does hint signs of excess absorption at the cores of the Na doublet and the K D_1 line, but not at significant levels. The K D_1 line is $\Delta R_p/R_\star = 0.0069 \pm 0.0035$ higher than the weighted mean of the two neighboring bands. The K D_2 line is unfortunately located in the telluric oxygen-A band. High-resolution transmission spectroscopy from ultra-stable radial velocity spectrographs like ESPRESSO is required to confirm this tentative evidence of excess absorption.

4. High-resolution data analysis

4.1. Rossiter-McLaughlin effect in radial velocities

The transit of a planet, blocking light from a part of the stellar disk, would introduce an asymmetric distortion in the line profiles of the stellar spectrum. The resulting radial velocity (RV) curves will exhibit an apparent anomaly known as the Rossiter-McLaughlin (RM; Rossiter 1924; McLaughlin 1924)

Table 6. Derived parameters from Rossiter-McLaughlin effect.

Parameter	Value
Systemic velocity #1, γ_1 [km s ⁻¹]	-89.4499 ± 0.0013
Systemic velocity #2, γ_2 [km s ⁻¹]	-89.4484 ± 0.0020
Systemic velocity #3, γ_3 [km s ⁻¹]	-89.4365 ± 0.0010
Proj. rotation velocity, $v \sin i_*$ [km s ⁻¹]	0.66 ± 0.14
Proj. spin-orbit angle, λ [deg]	8^{+26}_{-27}
RV semi-amplitude, K_* [km s ⁻¹]	0.0325 ± 0.0053
Offset to expected mid-transit, ΔT_C [d]	-0.0047 ± 0.0042
Limb darkening coeff., u_1, u_2	$0.3991, 0.2830$

effect. We collected the RVs from the three transits measured by the HARPS and HARPS-N pipelines, and jointly fit them with the ARoME library (Boué et al. 2013) implemented by a Python interface¹. ARoME can appropriately model the RM effect for the RVs derived from the CCF-based approach (e.g., HARPS). A circular orbit was adopted for WASP-21b (Bouchy et al. 2010). The combined RV model can be written as:

$$v_\star = v_{\text{RM}} + K_\star \sin[2\pi(t - T_C)/P] + \gamma, \quad (2)$$

where K_\star is the stellar RV semi-amplitude, T_C is the mid-transit time, P is the orbital period, and γ is the systemic RV. The RM anomaly v_{RM} is described by ARoME, which contains the following parameters: orbital period P , mid-transit time T_C , scaled semi-major axis a/R_\star , orbital inclination i , planet-to-star radius ratio R_p/R_\star , projected stellar rotation velocity $v \sin i_*$, projected spin-orbit angle λ , and quadratic limb-darkening coefficients (u_1, u_2). ARoME requires additional three parameters to define the line profile of CCF, that is, the width of a non-rotating star β_0 (adopted as 1.3 km s^{-1}), the width of the best Gaussian fit to out-of-transit CCF σ_0 (adopted as 2.9 km s^{-1}), and stellar macro-turbulence ζ (adopted as 2.3 km s^{-1}).

In the joint fitting of RV curves, the three transits shared the same values for K_\star , ΔT_C , $v \sin i_*$, and λ , but were allowed to have different values for γ . The offset to the predicted mid-transit time, ΔT_C , was calculated based on the ephemeris listed in Table 3, assuming that there is no transit timing variation. A Gaussian prior was imposed on ΔT_C , which has a width of three times the error propagation from the ephemeris. The values of P , a/R_\star , i , and R_p/R_\star were fixed to those listed in Table 3, and the limb-darkening coefficients were fixed to theoretical values (see Sect. 3.1). We employed emcee (Foreman-Mackey et al. 2013) to perform the MCMC process to search for the best-fit solutions. A rescaling multiple factor f_s for each night was used in the likelihood function to account for the over- or underestimation of error bars. In the end, the derived rescaling multiple factor was $1.07^{+0.20}_{-0.16}$ (transit #1), $1.25^{+0.25}_{-0.19}$ (transit #2), and $0.96^{+0.14}_{-0.11}$ (transit #3), respectively.

The joint analysis of the three transits resulted in a projected spin-orbit angle of $8^\circ^{+26}_{-27}$. Stars with photospheres cooler than $\sim 6100 \text{ K}$ in general have low obliquities (Winn & Fabrycky 2015). WASP-21 has an effective temperature of $T_{\text{eff}} = 5800 \pm 100 \text{ K}$ (Bouchy et al. 2010). The currently measured projected spin-orbit angle of $8^\circ^{+26}_{-27}$ seems to make WASP-21 follow this trend, but cautions should be taken given the large uncertainties. The derived stellar RV semi-amplitude of $32.5 \pm 5.3 \text{ m s}^{-1}$ is consistent with that derived from full-phase coverage RV curve without the RM anomaly in the discovery paper ($37.2 \pm 1.1 \text{ m s}^{-1}$;

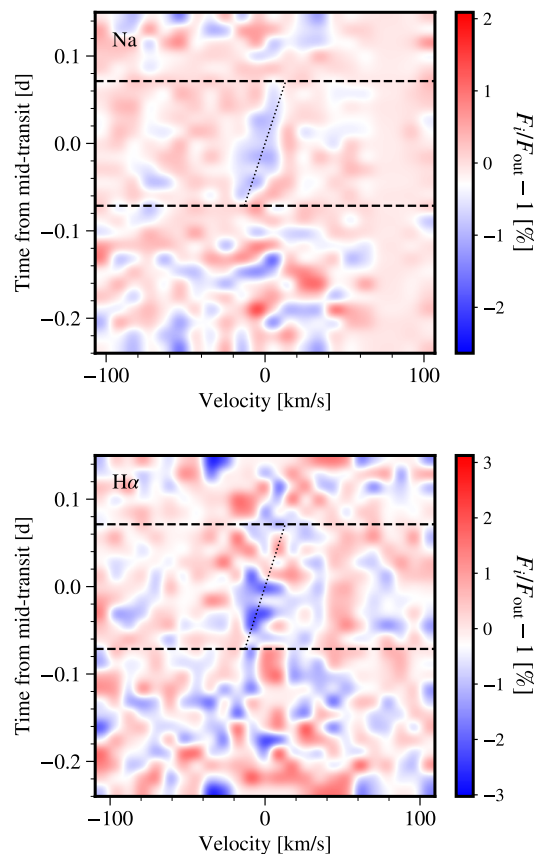


Fig. 7. Phase-resolved transmission spectrum at the Na (top) and H α (bottom) lines for WASP-21b. A radial velocity shift traced by the Na line center can be noticed during the transit event, which agrees with the radial velocity shift induced by the planet orbital motion. It is not clear at the H α line center.

Bouchy et al. 2010). The projected stellar rotation velocity measured from the RM effect ($0.7 \pm 0.1 \text{ km s}^{-1}$) is smaller than the spectroscopically derived value ($1.5 \pm 0.6 \text{ km s}^{-1}$; Bouchy et al. 2010). The discrepancy in the values of $v \sin i_*$ based on different methods have also been noticed in other planets and discussed by Brown et al. (2017) and Oshagh et al. (2018). The derived parameters are presented in Table 6. As shown in Fig. 6, the RV anomaly caused by the RM effect is relatively small.

4.2. Transmission spectroscopy of atomic lines

We followed the methodology detailed in Chen et al. (2020) to remove telluric and stellar lines in the acquired HARPS-N and HARPS spectra. In brief, the HARPS-N and HARPS spectra were first shifted back to the Earth's rest frame. Telluric H₂O and O₂ absorption lines were modeled and removed using the ESO software molecfit version 1.5.7 (Smette et al. 2015; Kausch et al. 2015). The telluric corrected spectra were then shifted to the stellar rest frame using barycentric Earth radial velocities and stellar radial velocities without the RM anomaly. The spectra were normalized and divided by the out-of-transit master (hereafter master-out) spectrum to remove stellar lines on a nightly basis. In this process, the continuum variation between individual exposures was corrected using a fourth-order polynomial function fitted on the individual-to-master-out flux-ratio spectra. And the master-out was constructed as the weighted mean of the out-of-transit spectra, using the square of S/N as weights. After

¹ <https://github.com/andres-jordan/PyARoME>

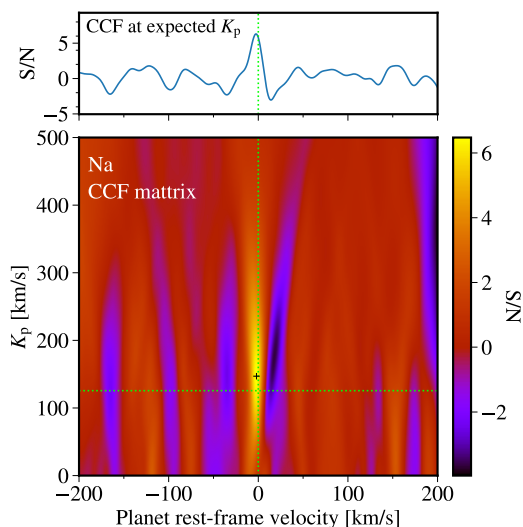


Fig. 8. Combined cross-correlation function (CCF) as a function of planet radial velocity (RV) semi-amplitude and RV shift of the Na doublet. The CCF has been expressed in the form of signal-to-noise ratio (S/N). The green dotted lines indicate the expected RV semi-amplitude and zero velocity. The black plus sign shows the location of the maximum CCF. *Top panel* shows the CCF at the expected RV semi-amplitude, corresponding to the horizontal green dotted line.

subtracting a value of one, the resulting residual spectra matrix is equivalent to a phase-resolved transmission spectrum.

The residual spectra in principle still contain distortion features of stellar lines introduced by the transit of a planet, during which a part of emergent stellar flux or radial velocity component are blocked. The Spectroscopy Made Easy tool (SME; Valenti & Piskunov 1996; Piskunov & Valenti 2017) was employed to create the models for center-to-limb variation (CLV) and Rossiter-McLaughlin (RM) effect. The simulated line distortion features caused by the CLV and RM effect were then corrected in the residual spectra. In the case of WASP-21, the CLV and RM effects are small and negligible (see Fig. B.1 and Fig. B.2). However, for completeness, the subsequent analysis has included the correction of both effects.

Figure 7 presents the phase-resolved transmission spectrum at the Na and H α lines in the stellar rest frame. To enhance S/N, the residual spectra of three nights have been combined and also binned in both time domain and velocity domain. Although the S/N is limited, it is still noticeable that the Na line center exhibits an excess absorption during the transit. The RV shift of the excess Na absorption during the transit is consistent with that induced by the planet orbital motion, indicative of a planetary origin. In contrast, the H α line center is dominated by noise.

In order to quantitatively assess the RV shift of the Na doublet excess absorption, the ideal way is to simultaneously fit the absorption profile at each time grid (e.g., Yan & Henning 2018; Casasayas-Barris et al. 2019). Given the low S/N of our current data set, we chose to perform the cross-correlation technique on the unbinned residual spectra using the best-fit doublet absorption model obtained on the combined transmission spectrum. The model template was shifted by a value of Δv_{abs} before its cross-correlation with the residual spectra that were fully in-transit. The cross-correlation functions (CCF) were then combined after they were shifted to planet rest frame using a grid of planet RV semi-amplitude values (K_p). The combined CCF at grids of K_p and Δv_{abs} is shown in Fig. 8, which is expressed in

Table 7. Parameters from the Gaussian fit to the Na line profile.

Parameter	Unit	Na D ₁	Na D ₂
<i>Free parameters</i>			
Line contrast	%	$0.84^{+0.16}_{-0.17}$	$1.18^{+0.23}_{-0.24}$
Line center	Å	$5895.851^{+0.029}_{-0.032}$	$5889.938^{+0.020}_{-0.021}$
Line FWHM	Å	$0.317^{+0.056}_{-0.050}$	$0.207^{+0.043}_{-0.039}$
Error multiple	–	$0.616^{+0.013}_{-0.013}$	
<i>Derived parameters</i>			
Effective radius	R_p	$1.307^{+0.054}_{-0.053}$	$1.414^{+0.072}_{-0.070}$
Center offset	km s ⁻¹	$-3.7^{+1.5}_{-1.6}$	$-0.7^{+1.0}_{-1.1}$
Line FWHM	km s ⁻¹	$16.1^{+2.9}_{-2.5}$	$10.5^{+2.2}_{-2.0}$

the form of S/N, that is, the CCF map has been normalized by the standard deviation of $|\Delta v_{\text{abs}}| = 100 - 200$ km s⁻¹ at a given K_p . The CCF map shows a maximum S/N of 6.5 at the location of $K_p = 147^{+61}_{-52}$ km s⁻¹ and $\Delta v_{\text{abs}} = -2^{+3}_{-4}$ km s⁻¹. The value of K_p is consistent with the predicted value of $K_p = 2\pi a \sin(i)/P = 125.6 \pm 3.8$ km s⁻¹ (assuming zero eccentricity and adopting parameters in Table 2), revealing that this excess absorption signal is related to the planet.

We created the final transmission spectrum at the atomic lines of interest (e.g., Na, H α , etc) by weighted combining the residual spectra obtained during fully in-transit, which have been shifted to the planet rest frame before the combination. The RV shift was performed using the expected planet RV semi-amplitude ($K_p = 125.6$ km s⁻¹). We fitted a Gaussian function to each atomic line to retrieve the line parameters such as contrast, center, and FWHM. The fitting procedure was implemented by the emcee package (Foreman-Mackey et al. 2013) with an error rescaling multiple, and the results were given in Table 7. The transmission spectrum at the Na doublet and H α lines is presented in Fig. 9, along with the best-fit models.

Excess absorption was only detected at the Na doublet. The derived line contrast is $0.84^{+0.16}_{-0.17}\%$ for Na D₁ and $1.18^{+0.23}_{-0.24}\%$ for Na D₂, respectively, resulting in a line ratio of $h_{D_2}/h_{D_1} = 1.41^{+0.46}_{-0.34}$, which is in line with previous studies on the other hot Jupiters (e.g., Žák et al. 2019, except for WASP-76b). The effective radius at the line center can be converted from the line contrast h as $R_{\text{eff}} = [1 + h/\mathcal{D}]^{1/2}$, where we adopted for $\mathcal{D} = R_p^2/R_\star^2$ the value of the 10 nm GTC/OSIRIS bandpass that Na was located in ($R_p/R_\star = 0.1087^{+0.0017}_{-0.0017}$). The effective radius at the centers of Na D₁ ($1.307^{+0.054}_{-0.053} R_p$) and D₂ ($1.414^{+0.072}_{-0.070} R_p$) are well below the Roche lobe radius $3.05^{+0.17}_{-0.16} R_p$, calculated according to Eggleton (1983). The line center of the Na doublet shows an average net blueshift of -1.6 ± 0.9 km s⁻¹, which might indicate a day-to-night planetary wind.

We did not detect any significant excess absorption at the H α line. A Gaussian fit with the center fixed at the laboratory wavelength would result in an excess absorption of $< 2.3\%$ at a confidence level of 95%, which is a rather loose constraint and indicates a noisy transmission spectrum at the H α line. We have examined the transmission spectrum at some other atomic lines that could serve as stellar activity indicators (e.g., Houdebine 2010; Yana Galarza et al. 2019). None of them showed any significant excess absorption, nor showed any significant features introduced by CLV and RM (see e.g., Fig. B.2). Therefore, the

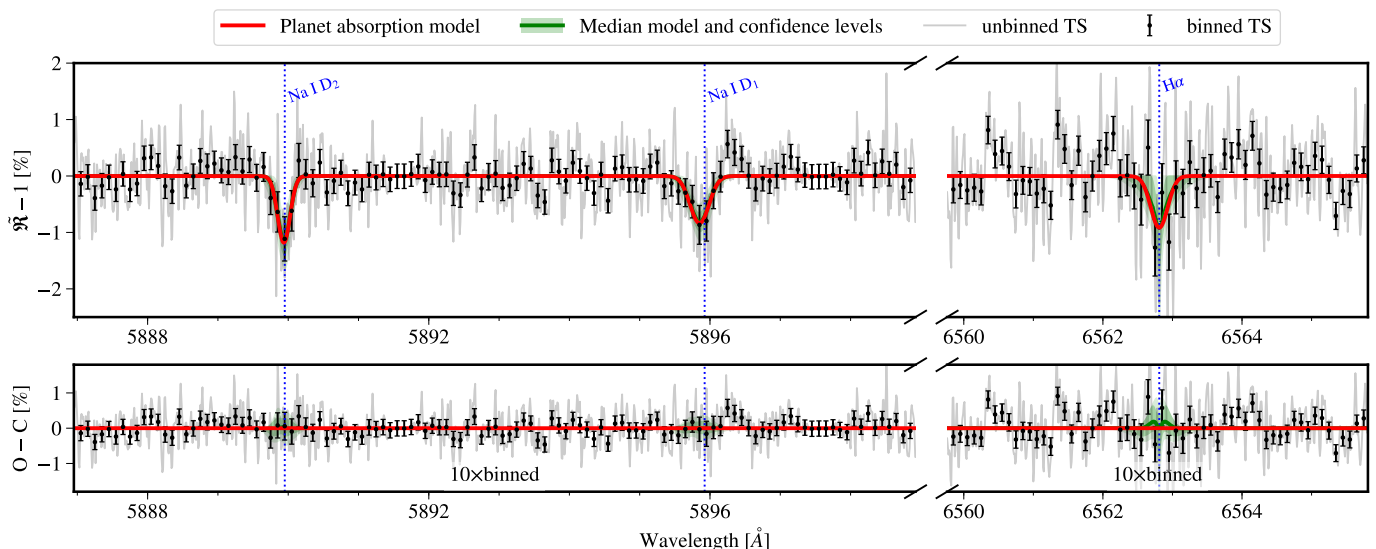


Fig. 9. High-resolution transmission spectrum of WASP-21b at the Na doublet and $H\alpha$ lines. The black circles with error bars show the 10×binned transmission spectrum, while the gray line shows the 0.01 Å version. The red line presents the best-fit Gaussian function to the Na doublet and $H\alpha$ lines. The green lines and shaded areas refer to the median and 1σ confidence region of the Gaussian fit. *Top panel* shows the transmission spectrum, while *bottom panel* shows the one after subtracting the best-fit model.

observed excess absorption at the Na doublet is unlikely a result of stellar activity or the CLV and RM effects.

Since the final transmission spectrum was created using the fully in-transit residual spectra, we performed the empirical Monte Carlo simulations (e.g., Redfield et al. 2008) to double check whether or not the excess absorption can only be detected in-transit. This was implemented by creating an in-transit (hereafter mock-in) and an out-of-transit mock data sets (hereafter mock-out), and performing the same analysis as the real data. Three scenarios were tested. In the “in-in” scenario, the real in-transit spectra were randomly divided into two groups, one as mock-in and the other as mock-out. In the “out-out” scenario, the real out-of-transit spectra were randomly divided. In the “in-out” scenario, mock-in spectra were randomly selected from the real in-transit spectra, while mock-out were from the real out-of-transit. The total number of mock-in and mock-out spectra was the same as that of the real data for both “in-in” and “out-out”, while the number was randomly generated but kept being no less than half of the real number for “in-out”. For all three scenarios, the mock in-to-out number ratio was kept being the same as the real number ratio. Once the two samples were ready, we created the mock transmission spectrum following the same way as aforementioned. We then measured the absorption depth within a defined passband bin centered at the target line on the transmission spectrum.

Figure 10 presents the resulting distributions for the Na doublet and $H\alpha$ lines. For the Na doublet, D_1 and D_2 were measured in two 0.35 Å passbands and averaged. We can only measure an excess absorption depth of $0.53 \pm 0.21\%$ in the “in-out” scenario, which is consistent with the value ($0.70 \pm 0.13\%$) measured on the real data. The “in-in” and “out-out” scenarios have posterior distributions centered at zero, indicating that either the signals have been canceled out or there is no signal. This confirms that the detected excess Na signal can only be detected in-transit. For $H\alpha$, it was measured in a 0.75 Å band, consistent with zero.

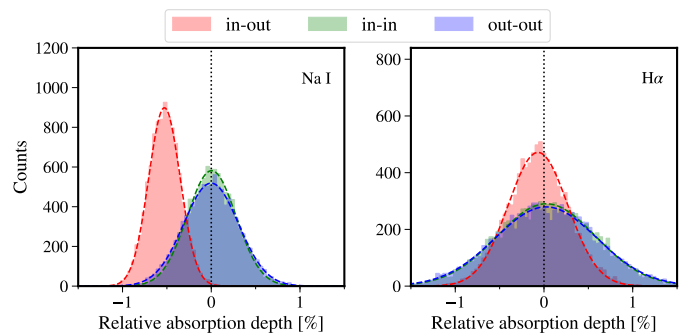


Fig. 10. Absorption depths measured in the mock transmission spectra created in the empirical Monte Carlo simulation (*left*: Na, *right*: $H\alpha$). The distribution of the scenarios “in-out”, “in-in”, and “out-out” are coded in red, green, blue colors, respectively. We refer the reader to Sect. 4.2 for details.

5. Discussion

5.1. The atmosphere of WASP-21b

With the flux calibrated low-resolution transmission spectrum acquired by GTC/OSIRIS, we have unambiguously detected a broad spectral signature centered at the Na doublet line. This signature indicates that the Na line wing is probably pressure-broadened, and that we are looking into relatively low altitudes of the atmosphere. The pressure broadening of the Na line has already been observed in several low-mass hot Jupiters, ranging from half-Jupiter-mass planets (WASP-96b, Nikolov et al. 2018; XO-2b, Pearson et al. 2019) to Saturn-mass planets (WASP-39b, Sing et al. 2016; Nikolov et al. 2016) and to sub-Saturn-mass planets (WASP-127b, Chen et al. 2018). The transmission spectrum of WASP-127b also exhibits a pressure broadening at the K doublet that is stronger than Na (Chen et al. 2018). For WASP-21b, we are not able to detect any significant pressure broadening at the K doublet, but do see a tentative evidence of excess absorption at the K D_1 line. The inference of pressure broadening of alkali lines indicates that the atmosphere is at least partially

clear, making the planet extremely favorable for further follow-up atmospheric characterization.

The high-resolution transmission spectrum of WASP-21b further confirms the presence of Na in its atmosphere at higher altitudes. This is achieved by resolving the radial velocity shift of the excess absorption at the Na doublet line, which is only detectable during the transit and consistent with the planet orbital motion. The excess absorption extends $\sim 28H$ at the Na D₁ line and $\sim 37H$ at the Na D₂ line, where $H = k_B T_{\text{eq}} / (\mu g_p) = 944$ km is the atmospheric scale height. This is much wider than the range covered by our GTC/OSIRIS low-resolution spectrum ($\sim 8H$). At high resolution, the extension of the excess absorption at Na (doublet averaged) has been measured to vary between $\sim 16H$ (WASP-127b, [Žák et al. 2019](#)) and $\sim 66H$ (WASP-49b, [Wytenbach et al. 2017](#)) for different hot Jupiters.

The Na doublet of WASP-21b exhibits a tentative net blueshift of -1.6 ± 0.9 km s⁻¹, indicative of a possible day-to-night planetary wind. This value is similar to wind velocities measured in the hot Jupiters HD 189733b ($-1.9^{+0.7}_{-0.6}$ km s⁻¹, [Louden & Wheatley 2015](#)) and WASP-49b (-1.7 ± 1.6 km s⁻¹, [Wytenbach et al. 2017](#)), which are also traced by Na. The Na-traced net velocities have also been reported for the hot Jupiter WASP-52b (-0.6 ± 0.7 km s⁻¹, [Chen et al. 2020](#)), and the ultra hot Jupiters KELT-9b ($+2.9 \pm 1.0$ km s⁻¹, [Hoeijmakers et al. 2019](#)) and MASCARA-2b (-3.1 ± 0.4 km s⁻¹, [Casasayas-Barris et al. 2019](#)). All of them refer to the doublet averaged value. The wind velocity and its variability, when measured precisely and phase-resolved, could be related to global circulation and drag strength (e.g., [Showman et al. 2013](#); [Kempton et al. 2014](#); [Flowers et al. 2019](#); [Komacek & Showman 2020](#)).

5.2. Pressure broadening in the atmospheres of hot Jupiters

To put the detected Na line broadening of WASP-21b in a general context of the hot Jupiter population, we define a line broadening metric (LBM) as follows:

$$\text{LBM} = \frac{1}{\mathcal{T}} \sum_{\lambda=-40 \text{ nm}}^{+40 \text{ nm}} \frac{\mathcal{D}_\lambda - \mathcal{D}_0}{\mathcal{D}_0} d\lambda, \quad (3)$$

where $d\lambda$ is the band width of a given passband in the low-resolution transmission spectrum, $\mathcal{T} = 2HR_p/R_\star^2$ is the expected transmission signal per scale height H , and $\mathcal{D}_0 = (R_p^2/R_\star^2)_0$ is the linearly interpolated continuum based on two 100 nm bands bracketing the 80 nm band centered at the Na line (or the K line). These three bands could be composed of different number of passbands, depending on how the literature studies were reporting their low-resolution transmission spectra. This metric becomes the Na or K equivalent width if a pressure-broadened Na or K line is detected. We measure LBM for all the hot Jupiters that have been studied by low-resolution transmission spectroscopy and that have sufficient wavelength coverage and passband resolution. In addition to LBM, we also calculate the local spectral slope α of these transmission spectra within the wavelength range of 510–900 nm, excluding two 80 nm bands centered at Na and K, by fitting a linear line in the $(\ln \lambda, R_p/R_\star)$ space, that is,

$$\alpha = \frac{1}{H} \frac{dR_p}{d \ln \lambda}. \quad (4)$$

The measured LBM for both Na and K and the local spectral slope α are given in Table 8.

To compare this observational metric to theoretical predictions, we then create a set of fiducial isothermal model transmission spectra using the Exo-Transmit code ([Kempton et al. 2017](#)), adopting WASP-21b's bulk parameters and covering temperatures from 650 K to 2650 K. The adopted gas opacities are: Na, K, TiO, VO, H₂O, CH₄, CO, CO₂. The other considerations include metallicities of 0.1×, 1×, 10×, and 100×solar, clouds at 10 mbar, 1 mbar or cloud-free, Rayleigh scattering enhanced by 1×, 10×, 1000×, and 10000×. We calculate LBM and spectral slope α for these models in the same way as the transmission spectrum data.

Figure 11 presents the distribution of 23 hot Jupiters collected from literature studies, along with WASP-21b. The left panels of Fig. 11 show the distribution on the plane of spectral slope versus LBM. Most hot Jupiters have the LBM values consistent with zero, indicative of no excess absorption within the 80 nm band centered at Na or K. Corresponding spectral slope varies from -9 to $+2$, which do not necessarily represent scattering features alone, because it is derived locally where absorption from molecules such as TiO and VO could bias it from a pure scattering slope. WASP-21b stands out with the largest Na LBM value, followed by WASP-96b ([Nikolov et al. 2018](#)) and XO-2b ([Pearson et al. 2019](#)). All these three hot Jupiters have shown clear pressure broadening at the Na line in low-resolution transmission spectra. This is consistent with the predictions of the fiducial models: the upper right corner is the location of hot Jupiters with clear atmospheres exhibiting significant alkali line broadening. On the other hand, only WASP-127b ([Chen et al. 2018](#)) shows a significant K LBM value, while the others have large uncertainties. The regions where TiO/VO-dominated atmospheres are predicted to locate, are free of any measurements. This is a natural result of the lack of TiO/VO detections in low-resolution optical transmission spectroscopy. The presence of clouds at higher altitudes or hazes introducing enhanced Rayleigh scattering would move the measurements towards zero LBM value.

The right panels of Fig. 11 show the distribution of hot Jupiters on the plane of surface gravity versus equilibrium temperature. They are assigned with colors according to the S/N of the measured LBM. The colormap is adjusted so that the white color is centered at $S/N = 3$. Consequently, the hot Jupiters with $S/N > 3$ would appear reddish. It is striking that the hot Jupiters with high significance of LBM have similar equilibrium temperatures, between ~ 1200 K and ~ 1500 K, and spanning a wide range of surface gravity values. WASP-21b is the one with the most significant LBM value, followed by WASP-96b, XO-2b, HD 209458b, WASP-127b, and WASP-39b. Indeed, in addition to WASP-21b, all other five hot Jupiters have been reported to have relatively clear atmospheres ([Nikolov et al. 2018](#); [Pearson et al. 2019](#); [MacDonald & Madhusudhan 2017](#); [Chen et al. 2018](#); [Wakeford et al. 2018](#)). Therefore, LBM can serve as a good indicator of pressure broadening of alkali lines, providing a new path to quantitatively compare the atmospheres of different hot Jupiters.

6. Conclusions

We observed one transit of the Saturn-mass planet WASP-21b with the low-resolution spectrograph OSIRIS at the 10.4 m GTC. We derived a transmission spectrum composed of 37 spectral bins with a uniform width of 10 nm. The most prominent spectral signature is a broad profile centered at the Na doublet, which is likely associated with the pressure broadening. The transmission spectrum shows a tentative evidence of excess absorption

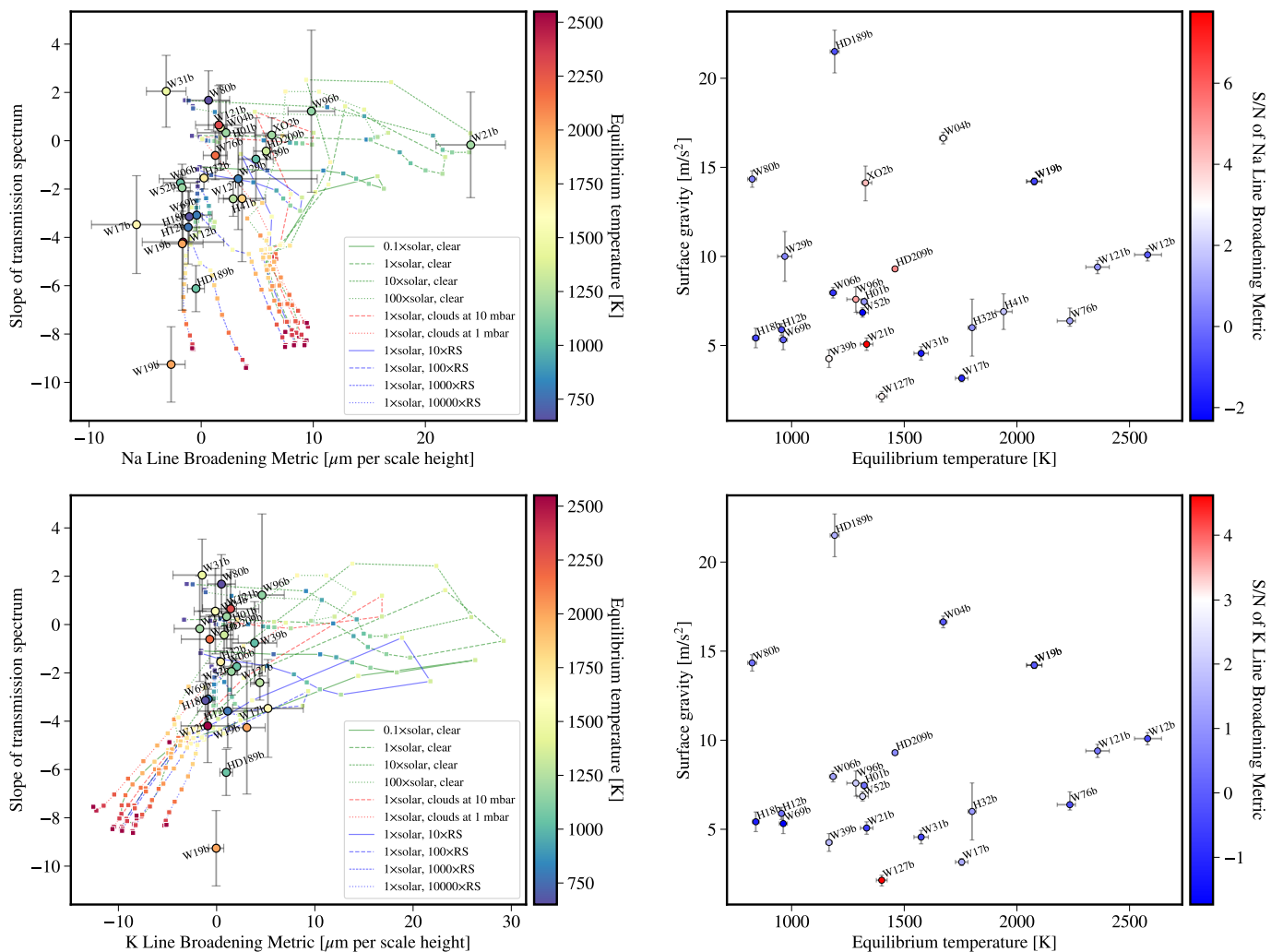


Fig. 11. *Left panels:* distribution of hot Jupiters characterized by low-resolution optical transmission spectroscopy on the plane of spectral slope versus line broadening metric. The first and second rows show the metric for Na and K, respectively. The colored lines show the corresponding values measured in the fiducial models, which connect models of different temperatures in the same group, that is, different metallicities, different cloud conditions, or different Rayleigh scattering (RS) enhancements. *Right panels:* distribution of the same hot Jupiters on the plane of planetary surface gravity versus equilibrium temperature. They are color coded by the signal-to-noise ratio (S/N) of the measured line broadening metric. The white part of the colorbar is centered at $S/N = 3$.

at the K D₁ line. We performed a spectral retrieval analysis on this transmission spectrum and reported the detection of Na at a confidence level of $>3.5\text{-}\sigma$. While a fiducial model leads to a Na detection at $3.5\text{-}\sigma$ significance, a simplified model provides a detection at $4.9\text{-}\sigma$ significance. The current data quality is not sufficient to constrain the chemical abundance and temperature structure precisely, for which high-precision follow-up observations are required.

We also observed one transit of WASP-21b with the high-resolution spectrograph HARPS-N at the 3.58 m TNG, and collected the archival data of another two transits observed by HARPS at the ESO 3.6 m telescope. The measured radial velocities exhibit a Rossiter-McLaughlin anomaly consistent with an aligned planetary orbit to stellar spin axis. We performed high-resolution transmission spectroscopy analysis and detected an excess absorption at the Na doublet. The resolved Na doublet shows a radial velocity shift during the transit that is consistent with the planet orbital motion, confirming its planetary origin. The Na doublet also exhibits a tentative net blueshift that might

hint a day-to-night wind. The data do not reveal any significant excess absorption at other atomic species.

With the data at hand, and comparing with literature results from other hot Jupiter observations, we proposed the line broadening metric (LBM) to quantify the excess absorption around the Na or K line in low-resolution optical transmission spectra. We measured the LBM values for 24 hot Jupiters that have been previously characterized by low-resolution optical transmission spectroscopy, and found that the hot Jupiters with high LBM values are likely to exhibit pressure-broadened Na line profiles. This slope-LBM diagram is the exoplanet version of color-color diagram, which can quantitatively distinguish the relatively clear atmospheres from others and thus help prioritize targets for observing campaigns. The metric of current hot Jupiter collection reveals that relatively clear atmospheres appear at equilibrium temperatures of 1200–1500 K. WASP-21b has the largest LBM value among the current collection. Together with the fact that Na is clearly detected in both low- and high-resolution transmission spectrum, WASP-21b is likely to have a relatively clear

Table 8. Measured line broadening metric and spectral slope for 24 hot Jupiters with low-resolution optical transmission spectroscopy.

Planet	$T_{\text{eq}}^{(a)}$ [K]	$g_{\text{p}}^{(a)}$ [m s ⁻¹]	$R_{\star}^{(a)}$ [R_{\odot}]	LBM(Na) [$\mu\text{m}/H$]	LBM(K) [$\mu\text{m}/H$]	$\alpha^{(b)}$	$H^{(c)}$ [R_{\star}]	$\mathcal{T}^{(d)}$ [ppm]	Reference
HAT-P-1b	1322 ⁺¹⁴ ₋₁₅	7.46 ^{+0.17} _{-0.17}	1.174	2.21 ± 2.55	1.02 ± 2.69	0.3 ± 1.3	0.0008	180	1
HAT-P-12b	955 ⁺¹¹ ₋₁₁	5.89 ^{+0.34} _{-0.34}	0.679	-1.16 ± 1.85	1.12 ± 3.06	-3.6 ± 1.5	0.0012	343	1, 2
HAT-P-18b	841 ⁺¹⁵ ₋₁₅	5.42 ^{+0.55} _{-0.55}	0.717	-1.07 ± 1.17	-1.14 ± 0.96	-3.1 ± 1.0	0.0011	303	3
HAT-P-32b	1801 ⁺¹⁸ ₋₁₈	6.00 ^{+1.60} _{-1.60}	1.225	0.25 ± 0.39	0.41 ± 0.37	-1.5 ± 0.5	0.0013	383	4, 5, 6, 7
HAT-P-41b	1941 ⁺³⁸ ₋₃₈	6.90 ^{+1.00} _{-1.00}	1.683	3.65 ± 2.10	–	-2.4 ± 2.6	0.0009	178	8
HD 189733b	1191 ⁺²⁰ ₋₂₀	21.50 ^{+1.20} _{-1.20}	0.752	-0.47 ± 0.75	0.98 ± 0.65	-6.1 ± 1.0	0.0004	120	1
HD 209458b	1459 ⁺¹² ₋₁₂	9.30 ^{+0.08} _{-0.08}	1.162	5.80 ± 1.12	0.76 ± 0.92	-0.4 ± 0.7	0.0007	170	1
WASP-4b	1673 ⁺¹⁷ ₋₁₇	16.64 ^{+0.33} _{-0.33}	0.910	1.72 ± 0.60	-0.13 ± 2.16	0.6 ± 1.8	0.0006	176	9
WASP-6b	1184 ⁺¹⁶ ₋₁₆	7.96 ^{+0.30} _{-0.30}	0.864	-1.85 ± 1.53	2.05 ± 1.55	-1.7 ± 0.3	0.0009	260	1
WASP-12b	2580 ⁺⁵⁸ ₋₆₂	10.09 ^{+0.35} _{-0.34}	1.657	-1.62 ± 3.63	-0.91 ± 2.72	-4.2 ± 1.5	0.0008	188	1
WASP-17b	1755 ⁺²⁸ ₋₂₈	3.16 ^{+0.20} _{-0.20}	1.583	-5.77 ± 4.02	5.22 ± 3.60	-3.5 ± 2.0	0.0018	454	1
WASP-19b	2077 ⁺³⁴ ₋₃₄	14.21 ^{+0.18} _{-0.18}	1.018	-2.69 ± 1.25	-0.04 ± 0.77	-9.3 ± 1.6	0.0007	211	10 ^(e)
WASP-19b	2077 ⁺³⁴ ₋₃₄	14.21 ^{+0.18} _{-0.18}	1.018	-1.69 ± 1.86	3.08 ± 1.87	-4.3 ± 2.8	0.0007	211	11 ^(e)
WASP-21b	1333 ⁺²⁸ ₋₂₈	5.07 ^{+0.35} _{-0.35}	1.136	24.04 ± 3.10	-1.72 ± 2.61	-0.2 ± 2.2	0.0012	251	12
WASP-29b	970 ⁺³² ₋₃₁	10.00 ^{+1.40} _{-1.40}	0.808	3.30 ± 7.05	–	-1.6 ± 2.1	0.0006	122	13
WASP-31b	1575 ⁺³² ₋₃₂	4.56 ^{+0.38} _{-0.38}	1.252	-3.12 ± 1.77	-1.47 ± 2.97	2.0 ± 1.5	0.0014	362	1
WASP-39b	1166 ⁺¹⁴ ₋₁₄	4.26 ^{+0.50} _{-0.50}	0.939	4.88 ± 1.55	3.86 ± 2.26	-0.8 ± 1.7	0.0015	421	1
WASP-52b	1315 ⁺²⁶ ₋₂₆	6.85 ^{+0.26} _{-0.26}	0.786	-1.70 ± 0.73	1.51 ± 0.65	-1.9 ± 1.0	0.0013	413	14, 15
WASP-69b	963 ⁺¹⁸ ₋₁₈	5.32 ^{+0.56} _{-0.56}	0.813	-0.40 ± 1.38	-0.86 ± 0.50	-3.1 ± 0.7	0.0011	307	16
WASP-76b	2235 ⁺⁵⁶ ₋₂₅	6.38 ^{+0.30} _{-0.72}	1.716	1.26 ± 1.07	-0.70 ± 2.90	-0.6 ± 1.0	0.0011	238	17
WASP-80b	825 ⁺²⁰ ₋₂₀	14.34 ^{+0.46} _{-0.46}	0.593	0.66 ± 1.88	0.49 ± 1.42	1.7 ± 1.2	0.0005	171	18
WASP-96b	1285 ⁺⁴⁰ ₋₄₀	7.59 ^{+0.73} _{-0.68}	1.050	9.83 ± 2.09	4.62 ± 2.27	1.2 ± 3.4	0.0008	195	19
WASP-121b	2358 ⁺⁵² ₋₅₂	9.40 ^{+0.37} _{-0.37}	1.458	1.57 ± 2.07	1.43 ± 2.87	0.7 ± 1.6	0.0009	233	20
WASP-127b	1400 ⁺²⁴ ₋₂₄	2.14 ^{+0.32} _{-0.28}	1.390	2.85 ± 0.87	4.40 ± 0.95	-2.4 ± 0.7	0.0024	492	21
XO-2b	1328 ⁺¹⁷ ₋₂₈	14.13 ^{+1.01} _{-0.94}	0.998	6.29 ± 1.48	–	0.2 ± 0.7	0.0005	102	22

Notes. ^(a) Equilibrium temperature T_{eq} , surface gravity g_{p} , and stellar radius R_{\star} are taken from TEPcat (Southworth 2011). ^(b) Scattering slope of the transmission spectrum between 510–900 nm, excluding two 80 nm bands centered at Na and K, respectively. ^(c) $H = k_{\text{B}}T_{\text{eq}}/\mu g_{\text{p}}$ is the atmospheric scale height, where $\mu = 2.3 \text{ g mol}^{-1}$ is assumed. ^(d) $\mathcal{T} = 2HR_{\text{p}}/R_{\star}^2$ is the transmission signal per scale height. ^(e) Due to discrepant results, the measurements for WASP-19b are listed individually, while weighted average values are presented for the other planets when multiple observations are available.

References. (1) Sing et al. (2016); (2) Wong et al. (2020); (3) Kirk et al. (2017); (4) Gibson et al. (2013b); (5) Mallonn & Strassmeier (2016); (6) Nortmann et al. (2016); (7) Alam et al. (2020); (8) Wakeford et al. (2020); (9) Huitson et al. (2017); (10) Sedaghati et al. (2017); (11) Espinoza et al. (2019); (12) This work; (13) Gibson et al. (2013a); (14) Chen et al. (2017b); (15) Alam et al. (2018); (16) Murgas et al. (2020); (17) Fu et al. (2020); (18) Parviainen et al. (2018); (19) Nikolov et al. (2018); (20) Evans et al. (2018); (21) Chen et al. (2018); (22) Pearson et al. (2019).

atmosphere, and thus will be an extremely interesting target for *James Webb* space telescope.

Acknowledgements. G. C. acknowledges the support by the B-type Strategic Priority Program of the Chinese Academy of Sciences (Grant No. XDB41000000), the Natural Science Foundation of Jiangsu Province (Grant No. BK20190110), and the Minor Planet Foundation of the Purple Mountain Observatory. This work is partly financed by the Spanish Ministry of Economics and Competitiveness through grant ESP2013-48391-C4-2-R. This work is based on observations made with the Gran Telescopio Canarias (GTC), installed at the Spanish Observatorio del Roque de los Muchachos of the Instituto de Astrofísica de Canarias, in the island of La Palma. This work is based on observations made with the Italian Telescopio Nazionale *Galileo* (TNG) operated on the island of La Palma by the Fundación Galileo Galilei of the INAF (Istituto Nazionale di Astrofisica) at the Spanish Observatorio del Roque de los Muchachos of the Instituto de Astrofísica de Canarias. This work is based on observations made with the Telescopio Nazionale *Galileo* (TNG) under Director's Discretionary Time of Spain's In-

stituto de Astrofísica de Canarias. This work has made use of Matplotlib (Hunter 2007) and the VizieR catalog access tool, CDS, Strasbourg, France (Ochsenbein et al. 2000). The authors thank the anonymous referee for their constructive comments on the manuscript.

References

- Alam, M. K., López-Morales, M., Nikolov, N., et al. 2020, *AJ*, 160, 51
Alam, M. K., Nikolov, N., López-Morales, M., et al. 2018, *AJ*, 156, 298
Allard, N. F., Spiegelman, F., & Kielkopf, J. F. 2016, *A&A*, 589, A21
Allard, N. F., Spiegelman, F., Leininger, T., & Molliere, P. 2019, *A&A*, 628, A120
Ambikasaran, S., Foreman-Mackey, D., Greengard, L., Hogg, D. W., & O'Neil, M. 2015, *IEEE Transactions on Pattern Analysis and Machine Intelligence*, 38, 252

- Asplund, M., Grevesse, N., Sauval, A. J., & Scott, P. 2009, *ARA&A*, 47, 481
- Barber, R. J., Strange, J. K., Hill, C., et al. 2014, *MNRAS*, 437, 1828
- Barros, S. C. C., Pollacco, D. L., Gibson, N. P., et al. 2011, *MNRAS*, 416, 2593
- Benneke, B. & Seager, S. 2012, *ApJ*, 753, 100
- Bouchy, F., Hebb, L., Skillen, I., et al. 2010, *A&A*, 519, A98
- Boué, G., Montalto, M., Boisse, I., Oshagh, M., & Santos, N. C. 2013, *A&A*, 550, A53
- Brown, D. J. A., Triaud, A. H. M. J., Doyle, A. P., et al. 2017, *MNRAS*, 464, 810
- Brown, T. M. 2001, *ApJ*, 553, 1006
- Buchner, J., Georgakakis, A., Nandra, K., et al. 2014, *A&A*, 564, A125
- Casasayas-Barris, N., Pallé, E., Yan, F., et al. 2019, *A&A*, 628, A9
- Chen, G., Casasayas-Barris, N., Pallé, E., et al. 2020, *A&A*, 635, A171
- Chen, G., Guenther, E. W., Pallé, E., et al. 2017a, *A&A*, 600, A138
- Chen, G., Pallé, E., Nortmann, L., et al. 2017b, *A&A*, 600, L11
- Chen, G., Pallé, E., Welbanks, L., et al. 2018, *A&A*, 616, A145
- Ciceri, S., Mancini, L., Southworth, J., et al. 2013, *A&A*, 557, A30
- Cosentino, R., Lovis, C., Pepe, F., et al. 2014, in *Society of Photo-Optical Instrumentation Engineers (SPIE) Conference Series*, Vol. 9147, Proc. SPIE, 91478C
- Crossfield, I. J. M. & Kreidberg, L. 2017, *AJ*, 154, 261
- Eastman, J., Siverd, R., & Gaudi, B. S. 2010, *PASP*, 122, 935
- Eggleton, P. P. 1983, *ApJ*, 268, 368
- Espinoza, N. & Jordán, A. 2015, *MNRAS*, 450, 1879
- Espinoza, N., Rackham, B. V., Jordán, A., et al. 2019, *MNRAS*, 482, 2065
- Evans, T. M., Sing, D. K., Goyal, J. M., et al. 2018, *AJ*, 156, 283
- Feroz, F., Hobson, M. P., & Bridges, M. 2009, *MNRAS*, 398, 1601
- Flowers, E., Brogi, M., Rauscher, E., Kempton, E. M. R., & Chiavassa, A. 2019, *AJ*, 157, 209
- Foreman-Mackey, D., Hogg, D. W., Lang, D., & Goodman, J. 2013, *PASP*, 125, 306
- Fortney, J. J. 2005, *MNRAS*, 364, 649
- Fu, G., Deming, D., Knutson, H., et al. 2017, *ApJ*, 847, L22
- Fu, G., Deming, D., Lothringer, J., et al. 2020, *arXiv e-prints*, arXiv:2005.02568
- Gandhi, S. & Madhusudhan, N. 2017, *MNRAS*, 472, 2334
- Gebek, A. & Oza, A. V. 2020, *arXiv e-prints*, arXiv:2005.02536
- Gibson, N. P., Aigrain, S., Barstow, J. K., et al. 2013a, *MNRAS*, 428, 3680
- Gibson, N. P., Aigrain, S., Barstow, J. K., et al. 2013b, *MNRAS*, 436, 2974
- Gibson, N. P., Aigrain, S., Roberts, S., et al. 2012, *MNRAS*, 419, 2683
- Griffith, C. A. 2014, *Philosophical Transactions of the Royal Society of London Series A*, 372, 20130086
- Heng, K. 2016, *ApJ*, 826, L16
- Heng, K. & Kitzmann, D. 2017, *MNRAS*, 470, 2972
- Hoeijmakers, H. J., Ehrenreich, D., Kitzmann, D., et al. 2019, *A&A*, 627, A165
- Houdebine, E. R. 2010, *MNRAS*, 403, 2157
- Huang, C., Arras, P., Christie, D., & Li, Z.-Y. 2017, *ApJ*, 851, 150
- Huitson, C. M., Désert, J. M., Bean, J. L., et al. 2017, *AJ*, 154, 95
- Hunter, J. D. 2007, *Computing in Science and Engineering*, 9, 90
- Iyer, A. R., Swain, M. R., Zellem, R. T., et al. 2016, *ApJ*, 823, 109
- Kausch, W., Noll, S., Smette, A., et al. 2015, *A&A*, 576, A78
- Kempton, E. M. R., Lupu, R., Owusu-Asare, A., Slough, P., & Cale, B. 2017, *PASP*, 129, 044402
- Kempton, E. M. R., Perna, R., & Heng, K. 2014, *ApJ*, 795, 24
- Kirk, J., Wheatley, P. J., Loudon, T., et al. 2017, *MNRAS*, 468, 3907
- Komacek, T. D. & Showman, A. P. 2020, *ApJ*, 888, 2
- Kreidberg, L. 2015, *PASP*, 127, 1161
- Kreidberg, L., Bean, J. L., Désert, J.-M., et al. 2014, *ApJ*, 793, L27
- Loudon, T. & Wheatley, P. J. 2015, *ApJ*, 814, L24
- MacDonald, R. J. & Madhusudhan, N. 2017, *MNRAS*, 469, 1979
- Madhusudhan, N. 2019, *ARA&A*, 57, 617
- Madhusudhan, N., Agúndez, M., Moses, J. I., & Hu, Y. 2016, *Space Sci. Rev.*, 205, 285
- Madhusudhan, N., Bitsch, B., Johansen, A., & Eriksson, L. 2017, *MNRAS*, 469, 4102
- Madhusudhan, N., Crouzet, N., McCullough, P. R., Deming, D., & Hedges, C. 2014, *ApJ*, 791, L9
- Madhusudhan, N. & Seager, S. 2009, *ApJ*, 707, 24
- Mallonn, M. & Strassmeier, K. G. 2016, *A&A*, 590, A100
- Mandel, K. & Agol, E. 2002, *ApJ*, 580, L171
- Mayor, M., Pepe, F., Queloz, D., et al. 2003, *The Messenger*, 114, 20
- McKemmish, L. K., Yurchenko, S. N., & Tennyson, J. 2016, *MNRAS*, 463, 771
- McLaughlin, D. B. 1924, *ApJ*, 60, 22
- Murgas, F., Chen, G., Nortmann, L., Pallé, E., & Nowak, G. 2020, *arXiv e-prints*, arXiv:2007.02741
- Nikolov, N., Sing, D. K., Fortney, J. J., et al. 2018, *Nature*, 557, 526
- Nikolov, N., Sing, D. K., Gibson, N. P., et al. 2016, *ApJ*, 832, 191
- Nortmann, L., Pallé, E., Murgas, F., et al. 2016, *A&A*, 594, A65
- Ochsenbein, F., Bauer, P., & Marcout, J. 2000, *A&AS*, 143, 23
- Oshagh, M., Triaud, A. H. M. J., Burdanov, A., et al. 2018, *A&A*, 619, A150
- Parviainen, H., Pallé, E., Chen, G., et al. 2018, *A&A*, 609, A33
- Patrascu, A. T., Yurchenko, S. N., & Tennyson, J. 2015, *MNRAS*, 449, 3613
- Pearson, K. A., Griffith, C. A., Zellem, R. T., Koskinen, T. T., & Roudier, G. M. 2019, *AJ*, 157, 21
- Pinhas, A., Madhusudhan, N., Gandhi, S., & MacDonald, R. 2019, *MNRAS*, 482, 1485
- Pinhas, A., Rackham, B. V., Madhusudhan, N., & Apai, D. 2018, *MNRAS*, 480, 5314
- Piskunov, N. & Valenti, J. A. 2017, *A&A*, 597, A16
- Rasmussen, C. E. & Williams, C. K. I. 2006, *Gaussian Processes for Machine Learning*
- Redfield, S., Endl, M., Cochran, W. D., & Koesterke, L. 2008, *ApJ*, 673, L87
- Richard, C., Gordon, I. E., Rothman, L. S., et al. 2012, *J. Quant. Spectr. Rad. Transf.*, 113, 1276
- Rossiter, R. A. 1924, *ApJ*, 60, 15
- Rothman, L. S., Gordon, I. E., Barber, R. J., et al. 2010, *J. Quant. Spectr. Rad. Transf.*, 111, 2139
- Sánchez, B., Aguiar-González, M., Barreto, R., et al. 2012, in *Society of Photo-Optical Instrumentation Engineers (SPIE) Conference Series*, Vol. 8446, Proc. SPIE, 84464T
- Schwenke, D. W. 1998, *Faraday Discussions*, 109, 321
- Seager, S. & Sasselov, D. D. 2000, *ApJ*, 537, 916
- Sedaghati, E., Boffin, H. M. J., MacDonald, R. J., et al. 2017, *Nature*, 549, 238
- Seeliger, M., Kitz, M., Errmann, R., et al. 2015, *MNRAS*, 451, 4060
- Seidel, J. V., Ehrenreich, D., Pino, L., et al. 2020, *A&A*, 633, A86
- Showman, A. P., Fortney, J. J., Lewis, N. K., & Shabram, M. 2013, *ApJ*, 762, 24
- Sing, D. K., Fortney, J. J., Nikolov, N., et al. 2016, *Nature*, 529, 59
- Smette, A., Sana, H., Noll, S., et al. 2015, *A&A*, 576, A77
- Southworth, J. 2011, *MNRAS*, 417, 2166
- Southworth, J. 2012, *MNRAS*, 426, 1291
- Stevenson, K. B. 2016, *ApJ*, 817, L16
- Tsiaras, A., Waldmann, I. P., Zingales, T., et al. 2018, *AJ*, 155, 156
- Valenti, J. A. & Piskunov, N. 1996, *A&AS*, 118, 595
- Žák, J., Kabáth, P., Boffin, H. M. J., Ivanov, V. D., & Skarka, M. 2019, *AJ*, 158, 120
- Wakeford, H. R., Sing, D. K., Deming, D., et al. 2018, *AJ*, 155, 29
- Wakeford, H. R., Sing, D. K., Kataria, T., et al. 2017, *Science*, 356, 628
- Wakeford, H. R., Sing, D. K., Stevenson, K. B., et al. 2020, *AJ*, 159, 204
- Welbanks, L. & Madhusudhan, N. 2019, *AJ*, 157, 206
- Welbanks, L., Madhusudhan, N., Allard, N. F., et al. 2019, *ApJ*, 887, L20
- Winn, J. N. & Fabrycky, D. C. 2015, *ARA&A*, 53, 409
- Wong, I., Benneke, B., Gao, P., et al. 2020, *AJ*, 159, 234
- Wytenbach, A., Lovis, C., Ehrenreich, D., et al. 2017, *A&A*, 602, A36
- Yan, F. & Henning, T. 2018, *Nature Astronomy*, 2, 714
- Yana Galarza, J., Meléndez, J., Lorenzo-Oliveira, D., et al. 2019, *MNRAS*, 490, L86
- Yurchenko, S. N., Barber, R. J., & Tennyson, J. 2011, *MNRAS*, 413, 1828
- Yurchenko, S. N. & Tennyson, J. 2014, *MNRAS*, 440, 1649

Appendix A: Additional figures for the GTC observation.

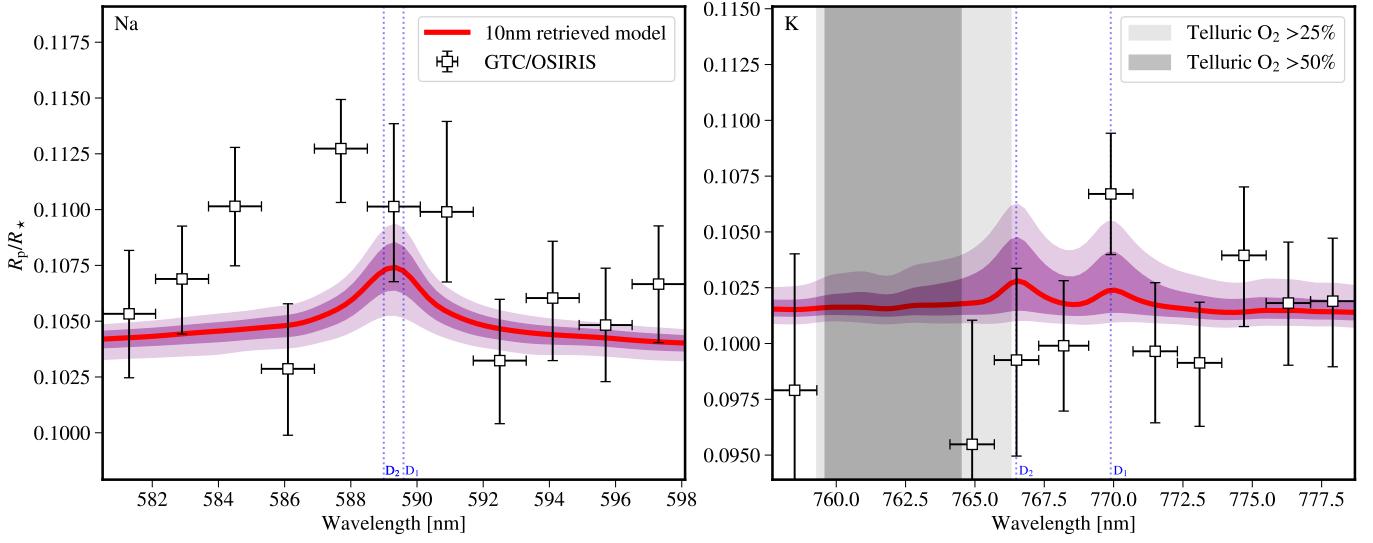


Fig. A.1. GTC/OSIRIS 16 Å bin transmission spectrum, zoomed at the Na (*left*) and K (*right*) doublets. The red line along with the purple shaded regions show the best model and its 1- σ /2- σ confidence levels retrieved from the 10 nm bin transmission spectrum. While it is too noisy to claim detections of the Na and K line cores, the data indeed hint possible excess absorption at the Na doublet and the K D₁ line. The K D₂ line is located in the telluric oxygen-A band.

Appendix B: Additional figures for the HARPS-N and HARPS observations.

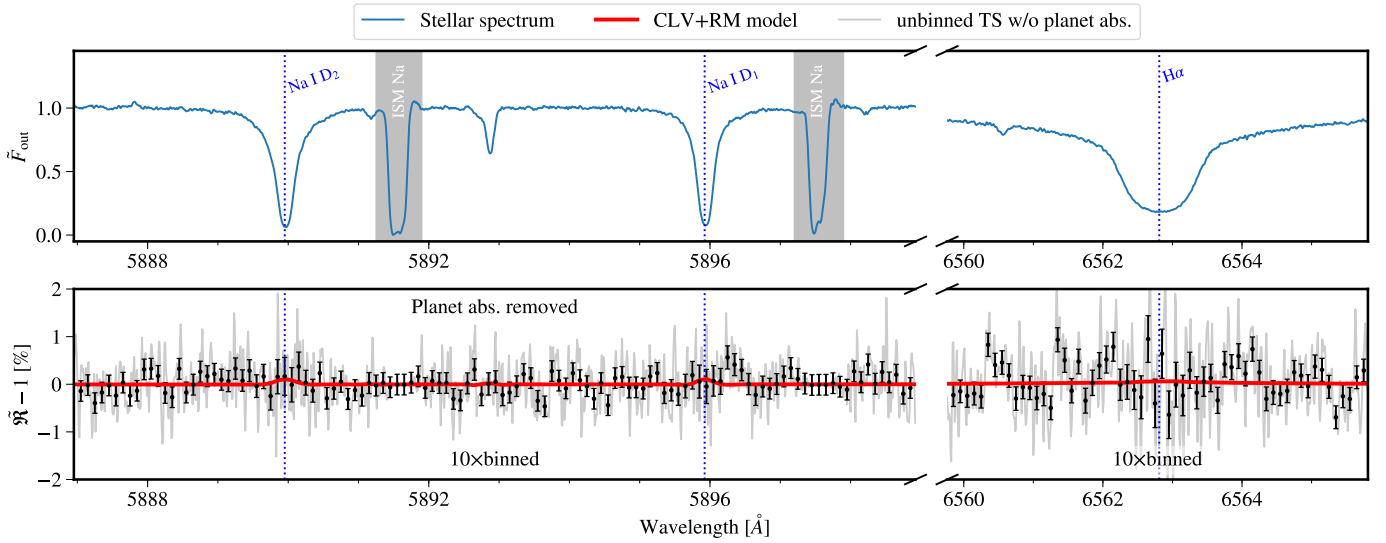


Fig. B.1. *Top panel:* out-of-transit master stellar spectrum at the Na doublet and H α lines. The strong interstellar Na absorption, indicated by the gray shadow, can be noticed on the red side of the stellar Na absorption. The wavelength is in the stellar rest frame. *Bottom panel:* transmission spectrum without the center-to-limb variation (CLV) and Rossiter-McLaughlin (RM) correction. The best-fit planet absorption presented in Fig. 9 has been removed. The red line shows the combined CLV and RM model.

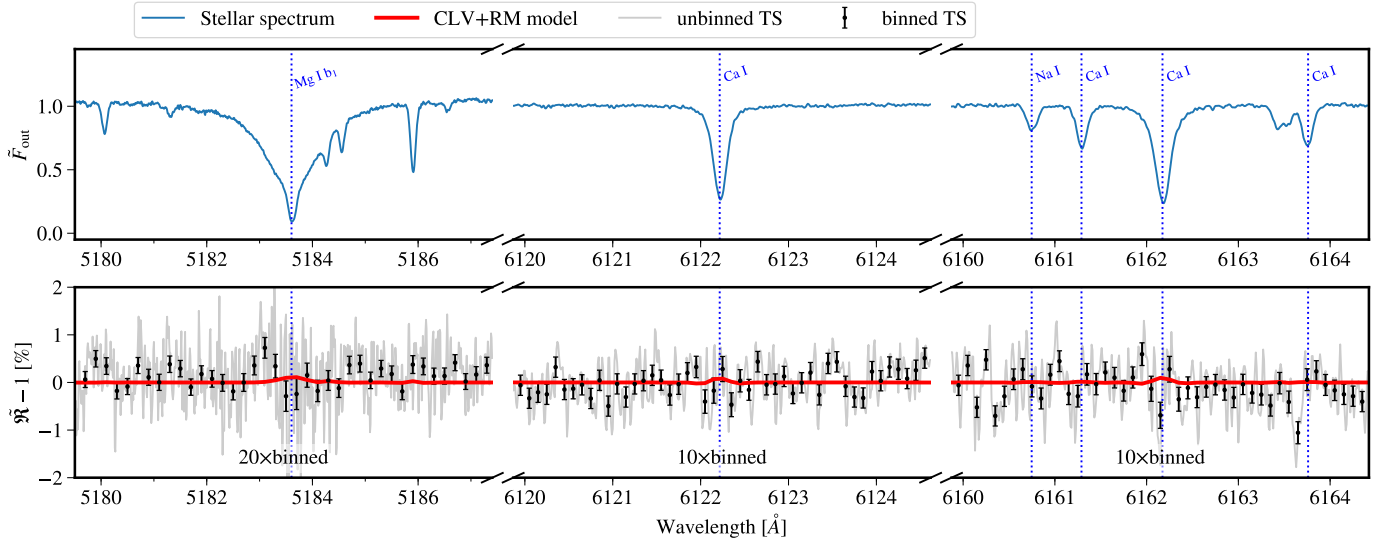


Fig. B.2. *Top panel:* out-of-transit master stellar spectrum at several stellar activity indicator lines. *Bottom panel:* transmission spectrum without the center-to-limb variation (CLV) and Rossiter-McLaughlin (RM) correction. Given the non-detection of excess absorption, no removal of planet absorption is performed. The red line shows the combined CLV and RM model.